

# The Gravitational Wave Background from Massive Black Hole Binaries in Illustris: spectral features and time to detection with pulsar timing arrays

Luke Zoltan Kelley<sup>1\*</sup>, Laura Blecha<sup>2</sup>, Lars Hernquist<sup>1</sup>, Alberto Sesana<sup>3</sup>

<sup>1</sup> *Harvard University, Center for Astrophysics*

<sup>2</sup> *University of Maryland*

<sup>3</sup> *University of Birmingham*

29 March 2022

## ABSTRACT

Pulsar Timing Arrays (PTA) around the world are using the incredible consistency of millisecond pulsars to measure low frequency gravitational waves from (super)Massive Black Hole (MBH) binaries. We use comprehensive MBH merger models based on cosmological hydrodynamic simulations to predict the spectra of a stochastic Gravitational-Wave Background (GWB). We use real Time-of-Arrival (TOA) specifications from the European, NANOGrav, Parkes, and International PTA (IPTA) to calculate realistic times to detection of the GWB across a wide range of model parameters. In addition to exploring the parameter space of environmental hardening rates (in particular: stellar scattering efficiencies), we have expanded our models to include eccentric binary evolution which can have a strong effect on the GWB spectrum. Our models show that strong stellar scattering and high characteristic eccentricities lead to higher GWB amplitudes and easier detections. While the GWB *amplitude* is degenerate between cosmological and environmental parameters, the location of a spectral turnover at low frequencies ( $f \lesssim 0.1 \text{ yr}^{-1}$ ) is strongly indicative of environmental coupling. At high frequencies ( $f \gtrsim 1 \text{ yr}^{-1}$ ), the GWB spectral index can be used to infer the number density of sources and possibly their eccentricity distribution. Even with pessimistic merger models, if the current rate of PTA expansion continues, we find that the International PTA (IPTA) is highly likely to make a detection within 10–15 years.

**Key words:** quasars: supermassive black holes, galaxies: kinematics and dynamics

## 1 INTRODUCTION

Pulsar Timing Arrays (PTA) are expected to detect Gravitational Waves (GW; Sazhin 1978; Detweiler 1979; Romani & Taylor 1983) from stable binaries of (super)-Massive Black Holes (MBH; Rajagopal & Romani 1995; Wyithe & Loeb 2003; Phinney 2001). These arrays use correlated signals in the consistently timed pulses from millisecond pulsars to search for low-frequency ( $\lesssim 10 \text{ yr}^{-1}$ ) perturbations to flat space-time (Hellings & Downs 1983; Foster & Backer 1990). There are currently three independent PTA searching for GW signals: the North-American Nanohertz Observatory for Gravitational waves (NANOGrav; McLaughlin 2013), the European PTA (EPTA; Kramer & Champion 2013), and the Parkes PTA (PPTA; Manchester et al. 2013). Additionally, the International PTA (IPTA, Hobbs et al. 2010) is a collaboration which aims to combine the data and expertise from each independent group.

Comparable upper limits on the presence of a stochastic Gravitational Wave Background (GWB) have been calculated by the

EPTA (Lentati et al. 2015), NANOGrav (Arzoumanian et al. 2015), PPTA (Shannon et al. 2015) and IPTA (Verbiest et al. 2016). These upper limits are already astrophysically informative in that much of the previously predicted parameter space is now in tension with observations, and there are suggestions that some models are excluded (Shannon et al. 2015). Many previous GWB models have assumed that most or all of the MBH pairs formed after the merger of their host galaxies are able to quickly reach the ‘hard binary’ phase ( $\lesssim 10 \text{ pc}$ ) and eventually coalesce due to GW emission (e.g. Wyithe & Loeb 2003; Jaffe & Backer 2003; Sesana 2013). These models, which assume GW-only driven evolution and produce purely power-law GWB spectra, are optimistic in that: 1) perhaps a substantial fraction of MBH Binaries stall before reaching the small separations ( $\sim 10^{-3}$ – $10^{-1} \text{ pc}$ ) corresponding to the PTA sensitive band (e.g. McWilliams et al. 2014); and 2) significant ‘attenuation’ of the GW signal may exist due to environmental processes (non-GW hardening, due to stellar scattering or coupling with a circumbinary gaseous disk) which decrease the amount of time binaries spend in a given frequency interval (e.g. Kocsis & Sesana 2011; Sesana 2013; Ravi et al. 2014; Rasskazov & Merritt 2016).

\* E-mail: lkelly@cfa.harvard.edu

Some recent GW-only models predict lower signal levels because of differing cosmological assumptions which produce different distributions of MBH binaries (e.g. [Roebber et al. 2016](#); [Sesana et al. 2016](#)), eliminating the tension with PTA upper limits. More comprehensive models have also been assembled which take into account binary-stalling and GW-attenuation (e.g. [Ravi et al. 2014](#)). Some of these models suggest that the GWB is only just below current observational sensitivities, which begs the question, ‘*how long until we make a detection?*’ Recently, PTA detection statistics conveniently formalized in [Rosado et al. \(2015\)](#) have been used by [Taylor et al. \(2016\)](#) to calculate times to detections for purely power-law, GW-only GWB models with a full range of plausible GWB amplitudes. [Vigeland & Siemens \(2016\)](#) also calculate detection statistics using a more extensive suite of broken power-laws to model the effects of varying environmental influences.

In [Kelley et al. \(2016, hereafter ‘KBH-16’\)](#) we construct the most comprehensive MBHB merger models to date, using the self-consistently derived population of galaxies and MBH from the Illustris cosmological, hydrodynamic simulations (§2.1, e.g. [Vogelsberger et al. 2014b](#); [Genel et al. 2014](#)). The MBHB population is post-processed using semi-analytic models of GW emission in addition to environmental hardening mechanisms that are generally *required* for MBHB to reach small separations within a Hubble time (e.g. [Begelman et al. 1980](#); [Milosavljević & Merritt 2003](#)), and emit GW in PTA-sensitive frequency bands.

In this paper, we introduce the addition of eccentric binary evolution to our models, and explore its effects on the GWB. To produce more realistic GWB spectra, we complement our previous semi-analytic (SA) calculations with a more realistic, Monte-Carlo (MC) technique. Using our merger models and resulting spectra, we calculate realistic times to detection for each PTA following [Rosado et al. \(2015\)](#) & [Taylor et al. \(2016\)](#). In §2 we describe our MBHB, GWB and PTA models. Then in §3 we describe the effects of eccentricity on binary evolution (§3.1) and the GWB spectrum (§3.2) including comparisons between the SA and MC calculations, and finally our predictions for times to GWB detections (§3.3).

## 2 METHODS

Our simulations use the coevolved galaxies and MBH particles from the Illustris cosmological, hydrodynamic simulations ([Vogelsberger et al. 2013](#); [Torrey et al. 2014](#); [Vogelsberger et al. 2014a](#); [Genel et al. 2014](#); [Sijacki et al. 2015](#)) run using the Arepo ‘moving-mesh’ code ([Springel 2010](#)). Our general procedure of extracting MBH, their merger events and their galactic environments are described in detail in [KBH-16](#). Here, we give a brief overview of our methods (§2.1) and the improvements made to include eccentric binary evolution (§2.2). We then describe the methods by which we calculate GW signatures (§2.3) and realistic detection statistics for simulated PTA (§2.4).

### 2.1 Illustris MBH Mergers and Environments

The Illustris simulation is a cosmological box of 106.5 Mpc on a side (at  $z = 0.0$ ) containing moving-mesh gas cells, and particles representing stars, dark matter, and MBH. All of the Illustris data is publicly available online ([Nelson et al. 2015](#)). MBH are ‘seeded’ with a mass of  $1.42 \times 10^5 M_{\odot}$  into halos with masses above  $7.1 \times 10^{10} M_{\odot}$  ([Sijacki et al. 2015](#)), where they accrete gas from the local environment and grow over time. As they develop, they proportionally deposit energy back into the local environment

([Vogelsberger et al. 2013](#)). When two MBH particles come within a gravitational smoothing length of one another (typically on the order of a kpc) a ‘merger’ event is recorded. From those mergers we identify the constituent MBH and the host galaxy in which they subsequently reside. From the host galaxy, density profiles are constructed which are used to determine the environment’s influence on the MBHB merger process. The simulations used here, as in [KBH-16](#), are semi-analytic models which integrate each binary (independently) from large-scale separations down to eventual coalescence based on prescriptions for GW- and environmentally- driven hardening.

### 2.2 Models for Eccentric Binary Evolution

We implement four distinct mechanisms which dissipate orbital energy and ‘harden’ the MBHB (as in [KBH-16](#)):

- **Dynamical Friction (DF)**, dominant on  $\sim$ kpc scales) is implemented following [Chandrasekhar \(1943\)](#) and [Binney & Tremaine \(1987\)](#), based on the local density (gas and dark matter) and velocity dispersion. The mass of the decelerating object is taken as the mass of the secondary MBH along with its host galaxy. We assume a model for tidal stripping such that the decelerating mass decreases as a power-law from the combined mass, to that of only the secondary MBH, over the course of a dynamical time<sup>1</sup>. With the addition of eccentric binary evolution, we make the approximation that DF does not noticeably affect the eccentricity distribution of binaries (e.g. [Colpi et al. 1999](#)), and that the semi-major axis remains the relevant distance scale. Equivalently, the “initial” eccentricities in our models can be viewed as the eccentricity once binaries enter the stellar scattering regime.
- **Stellar Loss-Cone (LC) scattering** ( $\sim$ pc), as implemented in [KBH-16](#), follows the theoretically-derived model from [Magorian & Tremaine \(1999\)](#) for a spherically-symmetric background of stars scattering with a central object. Scattering rates are calculated assuming isotropic, Maxwellian velocities and stellar distribution functions calculated from each galaxy’s stellar density profile<sup>2</sup>. Hardening rates depend on a dimensionless ‘refilling parameter’,  $\mathcal{F}_{\text{refill}} \in \{0.0, 1.0\}$ , which interpolates between a ‘steady-state’ LC ( $\mathcal{F}_{\text{refill}} = 0.0$ ), where equilibrium is reached between the scattering rate and refilling by the two-body diffusion of stars; and a ‘full’ LC ( $\mathcal{F}_{\text{refill}} = 1.0$ ), where the stellar distribution function is unaltered by the presence of the scattering source. In [KBH-16](#) our fiducial value was  $\mathcal{F}_{\text{refill}} = 0.6$ , in this analysis we explore six models with,  $\mathcal{F}_{\text{refill}} = [0.0, 0.2, 0.4, 0.6, 0.8, 1.0]$ . We refer to these as ‘*circular LC models*’.

To extend our results to eccentric binary systems, we have also implemented the LC scattering prescription from [Sesana et al. \(2006\)](#) & [Sesana \(2010\)](#) following the formalism of [Quinlan \(1996\)](#). Here the hardening rate ( $da/dt$ ) and eccentricity evolution ( $de/dt$ ) are determined by dimensionless constants  $H$  and

<sup>1</sup> The dynamical time used is that of the primary’s host galaxy. This corresponds to the ‘Enh-Stellar’ model from [KBH-16](#).

<sup>2</sup> Extended to unresolved  $\lesssim$  pc scales with power-law extrapolations. Additional details on Illustris stellar densities are included in §A.

$K$ , calculated in numerical scattering experiments such that,

$$\left. \frac{da}{dt} \right|_u \equiv -\frac{G\rho}{\sigma} a^2 H, \quad (1)$$

and

$$\left. \frac{de}{dt} \right|_u \equiv -\frac{G\rho}{\sigma} a H K. \quad (2)$$

We use the fitting formulae and tabulated constants from [Sesana et al. \(2006\)](#)<sup>3</sup>. Note that this semi-empirical approach, which we will refer to as ‘*eccentric LC models*’, explicitly assumes a full loss-cone in the scattering experiments by which they are calibrated. Using the eccentric model and imposing zero-eccentricity yields results very similar to the circular-only model, as expected.

- **Gas drag from a circumbinary, Viscous Disk (VD;  $\sim 10^{-3}$  pc)** is calculated following the thin disk models from [Haiman et al. \(2009\)](#). In these models, the disk is composed of three, physically distinct regions ([Shapiro & Teukolsky 1986](#)) determined by the dominant pressure (radiation versus thermal) and opacity (Thomson versus free-free) sources. From inner- to outer- disk, the regions are: 1) radiation & Thomson, 2) thermal & Thomson, and 3) thermal & free-free. The disk density profiles are constructed based on the self-consistently derived accretion rates given by Illustris, and truncated based on a (Toomre) gravitational stability criterion. Higher densities resulting from higher accretion rates lead to more extended inner-disk regions. We use an alpha-disk<sup>4</sup> throughout. It’s worth noting that the inner-disk region (1) has a very similar hardening curve to GW-emission:  $\tau_{\text{VD},1} \propto r^{7/2}$ , versus  $\tau_{\text{gw}} \propto r^4$ . In Illustris, post-merger MBH tend to have higher accretion rates, and thus larger inner-disk regions.

We assume that the disk has a negligible effect on the eccentric evolution of binaries, i.e.  $[de/dt]_{\text{VD}} = 0$ . This assumption is made for simplicity. While numerous studies have shown that eccentric evolution can at times be significant in circumbinary disks (e.g. [Armitage & Natarajan 2005](#); [Cuadra et al. 2009](#); [Roedig et al. 2011](#)), we are unaware of generalized descriptions of eccentricity evolution for binaries/disks with arbitrary initial configurations. In the analysis which follows, we explore a wide range of eccentricity parameter space. While a given model may end up being inconsistent with VD eccentric-evolution, the overall parameter space should still encompass the same resulting GWB spectra.

- **Gravitational Wave (GW) emission ( $\sim 10^{-5}$  pc)** hardens binaries at a rate given by [Peters \(1964, Eq. 5.6\)](#) as,

$$\frac{da}{dt} = -\frac{64 G^3 M_1 M_2 (M_1 + M_2)}{5 c^5 a^3} F(e), \quad (3)$$

where the eccentric enhancement,

$$F(e) \equiv \frac{\left(1 + \frac{73}{24} e^2 + \frac{37}{96} e^4\right)}{(1 - e^2)^{7/2}}. \quad (4)$$

In [KBH-16](#) we made the approximation that the eccentricity of all binaries was negligible and thus  $F(e) = 1$ . Here, we include models with non-zero eccentricity, evolved as ([Peters 1964,](#)

Eq. 5.7),

$$\frac{de}{dt} = -\frac{304 G^3 M_1 M_2 (M_1 + M_2)}{15 c^5 a^4} \frac{\left(e + \frac{121}{304} e^3\right)}{(1 - e^2)^{5/2}}. \quad (5)$$

### 2.3 Gravitational Waves from Eccentric MBH Binaries

Circular binaries, with (rest-frame) orbital frequencies  $f_r$ , emit GW monochromatically at  $2f_r$ , i.e. the  $n = 2$  harmonic. Eccentric systems lose symmetry, and emit at  $n = 1$  and all higher harmonics, i.e.  $f_h = n f_r$  (for  $n \in \mathbb{I}$ ). The GW energy spectrum can then be expressed as ([Enoki & Nagashima 2007, Eq. 3.10](#)),

$$\frac{d\mathcal{E}_{\text{GW}}}{df_r} = \sum_{n=1}^{\infty} \left[ L_{\text{GW,circ}}(f_h) \frac{\tau_h^f(f_h, e)}{n f_h} g(n, e) \right]_{f_h=f_r/n}. \quad (6)$$

The GW frequency-distribution function  $g(n, e)$  is shown in [Eq. B1](#). Equation (6) describes the GW spectrum emitted by a binary *over its lifetime*, which is used in the semi-analytic GWB calculation (§2.3.1). The total power radiated by an eccentric binary is enhanced by the factor  $F(e)$ , i.e.,  $L_{\text{GW}}(f_r, e) = L_{\text{GW,circ}}(f_r) \cdot F(e)$ , where the GW luminosity for a circular binary is ([Peters & Mathews 1963, Eq. 16](#)),

$$L_{\text{GW,circ}}(f_r) = \frac{32}{5 G c^5} (G M 2\pi f_r)^{10/3}. \quad (7)$$

Note that in [Eq. 6](#), the relevant timescale is the hardening-time (or ‘residence’-time) *in frequency*,

$$\tau_h^f \equiv \left| \frac{f}{df/dt} \right| = \frac{2}{3} \left| \frac{a}{da/dt} \right| \equiv \frac{2}{3} \tau_h, \quad (8)$$

which is 2/3 the hardening-time *in separation* (via Kepler’s law), which we use for most of our discussion and figures.

The GW strain from an individual, eccentric source can be related to that of a circular source as (e.g. [Amaro-Seoane et al. 2010, Eq. 9](#))<sup>5</sup>,

$$h_s^2(f_r) = \sum_{n=1}^{\infty} h_{\text{s,circ}}^2(f_h) \left(\frac{2}{n}\right)^2 g(n, e) \Big|_{f_h=f_r/n}. \quad (9)$$

Here, the GW strain from a circular binary is,

$$h_{\text{s,circ}}(f_r) = \frac{8}{10^{1/2}} \frac{(G M)^{5/3}}{c^4 d_L} (2\pi f_r)^{2/3} \quad (10)$$

(e.g. [Sesana et al. 2008, Eq. 8](#)), for a luminosity distance  $d_L$ , and a chirp mass  $\mathcal{M} = (M_1 M_2)^{3/5} / (M_1 + M_2)^{1/5}$ . Equation (9) describes the *instantaneous* GW strain amplitude from a binary, and is used in the Monte-Carlo GWB calculation (§2.3.2).

The GWB is usually calculated in one of two ways ([Sesana et al. 2008](#)): either Semi-Analytically (SA), treating the distribution of binaries as a smooth, continuous and deterministic function to calculate  $\partial^5 n_c(M_1, M_2, z, f_r, e) / \partial M_1 \partial M_2 \partial z \partial f_r \partial e$  ([Phinney 2001](#)), or alternatively, in the Monte Carlo (MC) approach, where  $n_c(M_1, M_2, z, f_r, e)$  is considered as a particular realization of a finite number of MBHB in the universe ([Rajagopal & Romani 1994](#)).

<sup>3</sup> [Sesana et al. \(2006\)](#): Eqs. 16 & 18, and Tables 1 & 3, respectively

<sup>4</sup> Where viscosity depends on both thermal and radiation pressure.

<sup>5</sup> Note the factor of  $(2/n)^2$  when converting from circular to eccentric systems.

### 2.3.1 Semi Analytic GWB

The GWB spectrum can be calculated from a distribution of eccentric binaries as (Enoki & Nagashima 2007, Eq. 3.11),

$$h_c^2(f) = \frac{4G}{\pi c^2 f} \int dM_1 dM_2 dz n_c(M_1, M_2, z) \sum_{n=1}^{\infty} \left[ L_{\text{GW,circ}}(f_r) \frac{\tau_h^f}{n f_r} g(n, e) \right]_{f_r=f(1+z)/n}, \quad (11)$$

where the summation is evaluated for all rest-frame frequencies with a harmonic matching the observed (redshifted) frequency bin  $f$ . Eq. 11 is derived by integrating the emission of each binary over its lifetime, which is assumed to happen quickly ( $\tau_h^f \ll \tau_{\text{Hubble}}$ ).

Each of the binaries in our simulation is evolved from their formation time (identified in Illustris) until coalescence. The GWB calculations only include the portions of the evolution which occur before redshift zero. In our implementation of the Eq. 11 calculation, interpolants are constructed for each binary's parameters (e.g. frequency, GW strain, etc) over its lifetime which are then used when sampling by simulated PTA.

### 2.3.2 Monte Carlo GWB

The GWB spectrum can also be constructed as the sum of individual source strains for all binaries emitting at the appropriate frequencies (and harmonics) in the observer's past light cone (Sesana et al. 2008, Eq. 6 & 10),

$$h_c^2(f) = \int dz dM \left[ \frac{d^3 N}{dz dM d \ln f_r} h_s^2(f_r) \right]_{f_r=f(1+z)} \quad (12)$$

$$= \int dz dM \frac{d^2 n_c}{dz dM} dV_c \left[ \frac{f_r}{df_r} h_s^2(f_r) \right]_{f_r=f(1+z)},$$

for a number of sources  $N$ , or comoving number-density  $n_c$  in a comoving volume  $V_c$ .

The differential element of the past light cone can be expressed as (e.g. Hogg 1999, Eq. 28),

$$dV_c(z) = 4\pi(1+z)^2 \frac{c}{H_0} \frac{d_c^2(z)}{E(z)} dz, \quad (13)$$

for a comoving distance  $d_c = d_L/(1+z)$ , redshift-zero Hubble constant  $H_0$ , and the cosmological evolution function  $E(z)$  (given in Eq. B3). The term  $f_r/df_r = f/df$ , which results from the definition of the characteristic strain as that over a logarithmic frequency interval, can be identified as the number of cycles each binary spends emitting in a given frequency interval (see Eq. B2).

To discretize Eq. 12 for a quantized number of sources (e.g. from a simulation) we convert the integral over number density, into a sum over sources within the Illustris comoving volume  $V_{\text{III}}$ ,

$$\int dz dM \dots \frac{d^2 n_c}{dz dM} dV_c \rightarrow \sum_{ij} \dots \frac{\Delta V_{ij}}{V_{\text{III}}}, \quad (14)$$

where the summation is over all binaries  $i$  at each time-step  $j$ . The factor  $\frac{\Delta V_{ij}}{V_{\text{III}}} \equiv \Lambda_{ij}$  represents the number of MBH binaries in the past light cone represented by each binary in the simulation<sup>6</sup>. The

<sup>6</sup>  $\Lambda_{ij}$  is equivalent to the multiplicative factors used in, for example, Sesana et al. (2008, Fig. 6) and effectively the same as in McWilliams et al. (2014).

volume of the past light cone represented by  $\Lambda_{ij}$  depends on the integration step-size, i.e.,

$$\Lambda_{ij} = \frac{1}{V_{\text{III}}} \frac{dV_c(z_{ij})}{dz_{ij}} \Delta z_{ij}, \quad (15)$$

where  $\Delta z_{ij}$  is the redshift step-size for binary  $i$  at time step  $j$ .  $\Lambda_{ij}$  is stochastic, determined by the number of binaries in a given region of the universe. Alternative 'realizations' of the universe can be constructed by, instead of using  $\Lambda_{ij}$  itself, scaling by a factor drawn from a Poisson distribution  $\mathcal{P}$ , centered at  $\Lambda_{ij}$ . Thus, to construct a particular realization of the GWB spectrum we calculate,

$$h_c^2(f) = \sum_{ij} \mathcal{P}(\Lambda_{ij}) \sum_{n=1}^{\infty} \left[ \frac{f_r}{\Delta f} h_s^2(f_r) \left( \frac{2}{n} \right)^2 g(n, e) \right]_{f_r=f(1+z)/n}. \quad (16)$$

## 2.4 Detection with Pulsar Timing Arrays

To calculate the detectability of our predicted GWB spectra, we use the detection formalism outlined by Rosado et al. (2015). A 'detection statistic'<sup>7</sup>  $X$  is constructed as the cross-correlation of PTA data using a filter which maximizes the Detection Probability (DP)  $\gamma$ . The optimal filter is known to be the 'overlap reduction function' (Finn et al. 2009) which, for PTA, is the Hellings & Downs (1983) curve that depends on the particular PTA configuration (angular separation between each pair of pulsars). Using the optimal detection statistic, and the noise characteristics of the PTA under consideration, parameters like the signal-to-noise ratio (SNR; and SNR-threshold) or DP can be calculated based on a GWB. Rosado et al. (2015) should be consulted for the details of the detection formalism but, for completeness, the relevant equations used in our calculations are included in §B1.

Following Rosado et al. (2015) and Taylor et al. (2016) we construct simulated PTA using published specifications of the constituent pulsars. We then calculate the resulting DP (Eq. B12) for our model GWB against each PTA, focusing on the varying time to detection. We consider models for all PTA:

- European<sup>8</sup> (EPTA, Desvignes et al. 2016; Caballero et al. 2016)
- NANOGrav<sup>9</sup> (The NANOGrav Collaboration et al. 2015),
- Parkes<sup>10</sup> (EPTA, Shannon et al. 2015; Reardon et al. 2016),
- International<sup>11</sup> (IPTA, Verbiest et al. 2016; Lentati et al. 2016).

For each array we include an 'expanded' model (denoted by '+') including the addition of a pulsar every  $X$  years, where for the individual PTA,  $X = 1/4$ , and for the IPTA,  $X = 1/6$  (Taylor et al. 2016). All expanded pulsars are given a TOA accuracy of 250 ns, and a random sky location. The public PTA specifications include observation times for each TOA of all pulsars in the array. We take the first TOA as the start time of observations for the corresponding pulsar, and use the overall number of calendar days with TOA measurements<sup>12</sup> to determine the characteristic observing cadence.

Detection statistics depend on pairs of pulsars. For each pair, we set the observational duration as the stretch of time over which both pulsars were being observed:  $T_{ij} = T_i \cap T_j$ ; and take the

<sup>7</sup> i.e. measure of signal strength in PTA (mock) data.

<sup>8</sup> [http://www.epta.eu.org/aom/EPTA\\_v2.2\\_git.tar](http://www.epta.eu.org/aom/EPTA_v2.2_git.tar)

<sup>9</sup> <https://data.nanograv.org/>

<sup>10</sup> <http://doi.org/10.4225/08/561EFD72D0409>

<sup>11</sup> [http://www.ipta4gw.org/?page\\_id=519](http://www.ipta4gw.org/?page_id=519)

<sup>12</sup> Grouping TOA by observation day deals with near-simultaneous observations at different frequencies which are not representative of the true observing cadence.

characteristic cadence as the maximum from that of each pulsar:  $\Delta t_{ij} = \max(\Delta t_i, \Delta t_j)$ . The sensitive frequencies for each pair is then determined by Nyquist sampling with  $\Delta f_{ij} = 1/T_{ij}$ , such that each frequency  $f_{ijk} = 1/T_{ij} + k/\Delta t_{ij}$ , and  $f \in [1/T, 1/\Delta t]$ . In calibrating the  $\lambda_{\text{noise}}$  parameter, we take the end time of observations as 2015/01/01, while for calculations of time to detection, we start with an end point of 2017/01/01.

Pulsars are characterized by a (white-noise) standard deviation  $\sigma_i$  in their TOA. For a time interval  $\Delta t$ , the white-noise power spectrum  $P_{w,i}$  is given by,

$$P_{w,i} = 2\sigma_i^2 \Delta t. \quad (17)$$

Some pulsars in the public PTA data provide specifications for a red-noise term<sup>13</sup> which we also include. We assume that when red-noise specifications are not provided that they are negligible.

To calibrate our calculations to the more comprehensive analyses employed by the PTA groups themselves, we rescale the white noise ( $\sigma_i$ ) of each pulsar by a factor  $\lambda_{\text{noise}}$  (the procedure described in Taylor et al. 2016). To determine  $\lambda_{\text{noise}}$ , we calculate upper-limits on the GWB amplitude  $A_{\text{yr}^{-1},\text{ul}}$  (Taylor et al. 2016, Eq. 4), with a ‘true’ (i.e. injected) GWB amplitude of  $A_{\text{yr}^{-1}} = 0.6 \times 10^{-15}$ , and iteratively adjust  $\lambda_{\text{noise}}$  until the calculated  $A_{\text{yr}^{-1},\text{ul}}$  matches the published values. The total noise used in our calculations is then<sup>14</sup>,

$$P_i = \lambda_{\text{noise}}^2 P_{w,i} + P_{r,i}. \quad (18)$$

Detailed specifications of each PTA configuration are included online as JSON files. The basic parameters of each individual array and the IPTA are summarized in Table 1. The values of  $\lambda_{\text{noise}}$  say something about how consistent the overall noise-parameters are with the upper-limits calculated *in our framework*. Values of  $\lambda_{\text{noise}} > 1$  suggest that additional noise is required. Out of the individual PTA, the European requires the largest  $\lambda_{\text{noise}}$  which may be related to the relatively few pulsars with red-noise specifications (8 out of 42). Parkes, with the longest observational durations (and thus the most low-frequency leverage on pulsar power-spectra), has the most pulsars with red-noise models (15 out of 20), which seems to create an over-estimation of the effective total noise in the system.

The International PTA requires the largest  $\lambda_{\text{noise}}$ , more than twice as large as any individual PTA, suggesting that the noise is under estimated, or that the calculated upper-limit is sub-optimal—again, likely due to systematics from combining data from not only numerous telescopes, but numerous groups and/or methodologies. To address this issue we also present our results analyzed against an alternative ‘IPTA’’. The IPTA’ is constructed by manually combining the TOA from the individual arrays but without re-calibrating the overall result. White noise parameters are added in quadrature, using the  $\lambda_{\text{noise}}$  from each PTA. When a pulsar has multiple red-noise models from different groups, we use the model from the group with the most TOA. While the total number of pulsars across all PTA is actually 68, we only include those from the official IPTA specification as the additional 19 pulsars produce a  $\lesssim 1\%$  improvement in the resulting statistics. In effect, IPTA’ assumes that each

Name	N	Red	Medians (Pulsars / Pairs)			$\lambda_{\text{noise}}$
			$\sigma$ [ $\mu\text{s}$ ]	Dur. [yr]	Cad. [day]	
European	42	8	6.5 / 6.9	12.3 / 10.9	14 / 20	3.14
NANOGrav	37	10	1.8 / 1.8	8.8 / 5.5	23 / 38	1.41
Parkes	20	15	1.8 / 1.8	21.2 / 14.9	21 / 15	0.75
International / IPTA	49	16	3.6 / 3.4	15.5 / 11.6	15 / 23	6.63
IPTA’	49	22	3.4 / 3.2	15.5 / 11.0	12 / 20	1.0

**Table 1.** Summary of parameters for the individual and International PTA used in our calculations. The first and second columns give the number of pulsars (N) and the number which include a red-noise model (Red). The following three columns—the noise ( $\sigma$ ), and observational duration & cadence—are each given as median value for ‘pulsars/pulsar-pairs’. Durations are calculated using the first TOA given in the public PTA specifications, and taking the end time as as 2017/01/01. The observing cadence is calculated based on the total number of days with TOA entries between the first and last recorded observations. The IPTA’ is the manual combination of specifications from each individual PTA, without calibrating to any published upper-limit (i.e.  $\lambda_{\text{noise}} \equiv 1.0$ ).

individual PTA can be optimally combined, without any efficiency losses.

<sup>13</sup> Models for each PTA are: European—Caballero et al. (2016, Eq.3); NANOGrav—The NANOGrav Collaboration et al. (2015, Eq.4); Parkes—Reardon et al. (2016, Eq.4); International—Lentati et al. (2016, Eq.10). Note that for the red-noise amplitudes included in the IPTA public data release, the frequency  $f$  must be given in  $\text{yr}^{-1}$ , and the duration  $T$  in yr (for Eq.10 of Lentati et al. 2016).

<sup>14</sup> In the presence of red-noise the power spectrum is frequency dependent, i.e.  $P_{ik} = P_i(f_k)$ , but we suppress the additional subscript for convenience.

### 3 RESULTS

#### 3.1 Eccentric Evolution

For a given simulation, all binaries are initialized with the same eccentricity and are let to evolve with dynamical friction (DF), loss-cone (LC) stellar scattering, drag from a circumbinary Viscous-Disk (VD), and Gravitational Wave (GW) hardening. LC increases initially-nonzero eccentricities, and GW emission decreases them. In our models we assume DF & VD do not affect the eccentricity distribution. The upper panels of Fig. 1 show the resulting binary eccentricity evolution versus orbital frequency (a) and binary separation (b) for our entire population of MBHB. Solid lines show median values at each separation, and colored bands show the surrounding 68%. Binaries initialized to  $e_0 = 0.0$  stay at zero, but the population initialized to only  $e_0 = 0.01$  have a median roughly ten times larger at  $r \sim 1$  pc, and still  $e \gtrsim 0.05$  at orbital frequencies of  $1 \text{ yr}^{-1}$ .

Binaries which are both *heavy* ( $M > 10^9 M_\odot$ ) and *major* ( $\mu > 0.1$ ) tend to dominate the GWB signal (Kelley et al. 2016). The eccentricity evolution of this subset of binaries is shown separately in panels (c) & (d) of Fig. 1. The eccentricities of these systems tend to dampen more quickly at separations below  $\sim 1$  pc. In general, this leads to much lower eccentricities at PTA frequencies for the *heavy & major* population. In the  $e_0 = 0.95$  model, for example, the *heavy & major* median eccentricity drops below 0.6 by  $f = 0.1 \text{ yr}^{-1}$  (panel c), whereas it takes until  $f \sim 3 \text{ yr}^{-1}$  for the population of all binaries (panel a). In terms of separation, most of the  $e_0 = 0.95$  population has  $e \lesssim 0.5$  by  $r \sim 10^{-2}$  pc, whereas for all binaries the same isn't true until  $r \sim 10^{-4}$  pc. The highest eccentricity model,  $e_0 = 0.99$ , behaves somewhat differently, as it tends to in many respects. For  $e_0 = 0.99$ , binaries pass through most of the PTA band before their eccentricities are substantially damped in both the overall and *heavy & major* groups.

Once binaries begin to approach the PTA sensitive band ( $f \gtrsim 10^{-2} \text{ yr}^{-1}$ ) the eccentricity distributions are always monotonically decreasing. At the corresponding separations, GW becomes more and more dominant to LC, but at the same time, VD can still be an important hardening mechanism. If circumbinary disks can be effective at increasing eccentricity, or if a resonant third MBH were present, eccentricities could still be excited in the PTA regime. Either of these effects may be important for some MBHB systems, but likely not for the overall population.

In our models, while binary eccentricity is evolved by both LC and GW hardening, the eccentricity distribution itself only affects the rate of *semi-major-axis* hardening (i.e.  $da/dt$ , Eq. 3) by the GW mechanism. As eccentricity increases, GW hardening becomes more effective. The hardening time ( $a/[da/dt]$ ) for all binaries is plotted in the upper panels of Fig. 2. The frequency panel (a) has been extended to show more of the physical picture, with the PTA-relevant regime shaded in grey. The DF regime goes from large separations down to  $r \sim 50$  pc, and according to our prescription includes no eccentricity dependence.

The relatively flat portion of the hardening curve between  $r \sim 50$  pc and  $r \sim 2 \times 10^{-2}$  pc (panel b) is typically the LC-dominated regime. Ignoring the radial dependence of galactic  $\rho/\sigma$  (density/velocity) profiles, the hardening rate should scale like  $\tau_h \propto a^{-1}$  (see Eq. 1). The hardening rates in panel b, however, show the convolution over many orders of magnitude in total-mass and mass-ratio, flattening the hardening curves. The scaling is more clear for the low-eccentricity models of the *heavy & major* subset (panel d) which show more canonical LC hardening rates between  $r \sim 10$  pc and  $r \sim 1$  pc.

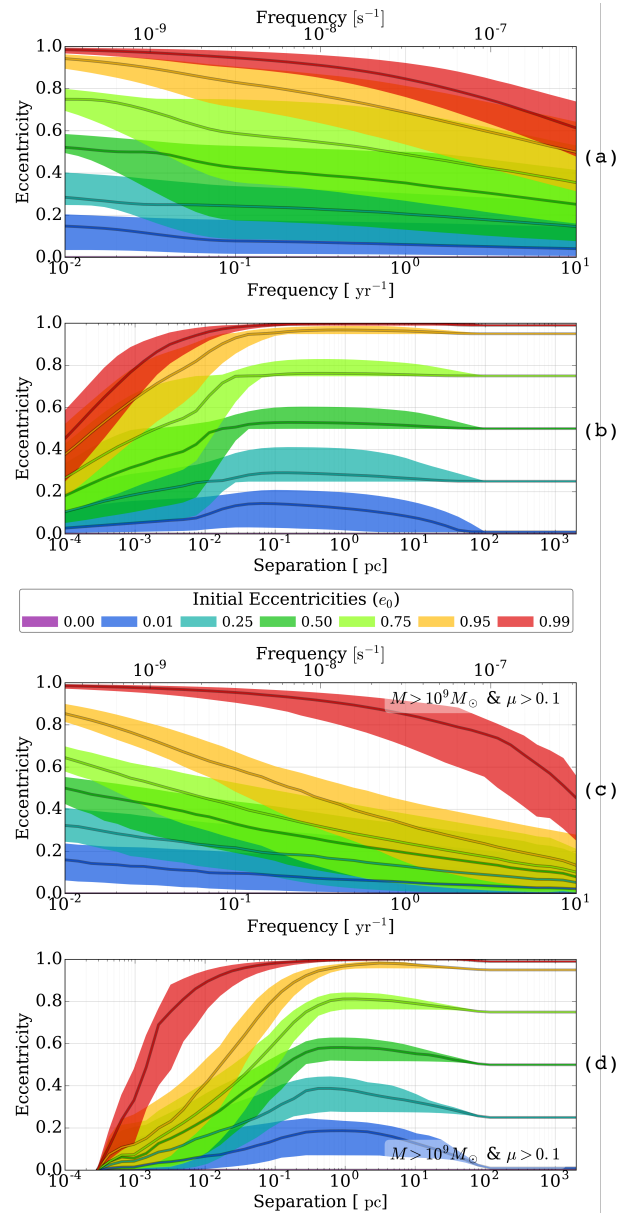


**Figure 1.** Evolution of eccentricity versus separation (panels a & c) and orbital frequency (panels b & d) for a variety of initial eccentricities. The upper panels (a & b) show eccentricities for all binaries, while the lower panels (c & d) show only the *heavy* ( $M > 10^9 M_\odot$ ) and *major* ( $\mu > 0.1$ ) subset which tend to dominate the GWB. Each band corresponds to 68% of the population, and the central lines to the medians.

Even at these large separations, the hardening timescale is significantly decreased for the highest initial eccentricities:  $e_0 = 0.95$  and especially  $e_0 = 0.99$ . In these models, GW emission begins to play an important role in hardening much earlier in the systems' evolution. The dashed vertical lines in Fig. 2 show the frequency and separation at which GW hardening becomes dominant over DF and LC<sup>1</sup> in 50% of systems. For  $e_0 = 0.99$ , GW domination occurs at

<sup>1</sup> Note that VD can be dominant for an additional decade of frequency or separation, but because the amplitude and power-law index of VD are very similar to that of GW hardening, the transition points plotted are more representative of a change in hardening rate and/or GWB spectral shape.

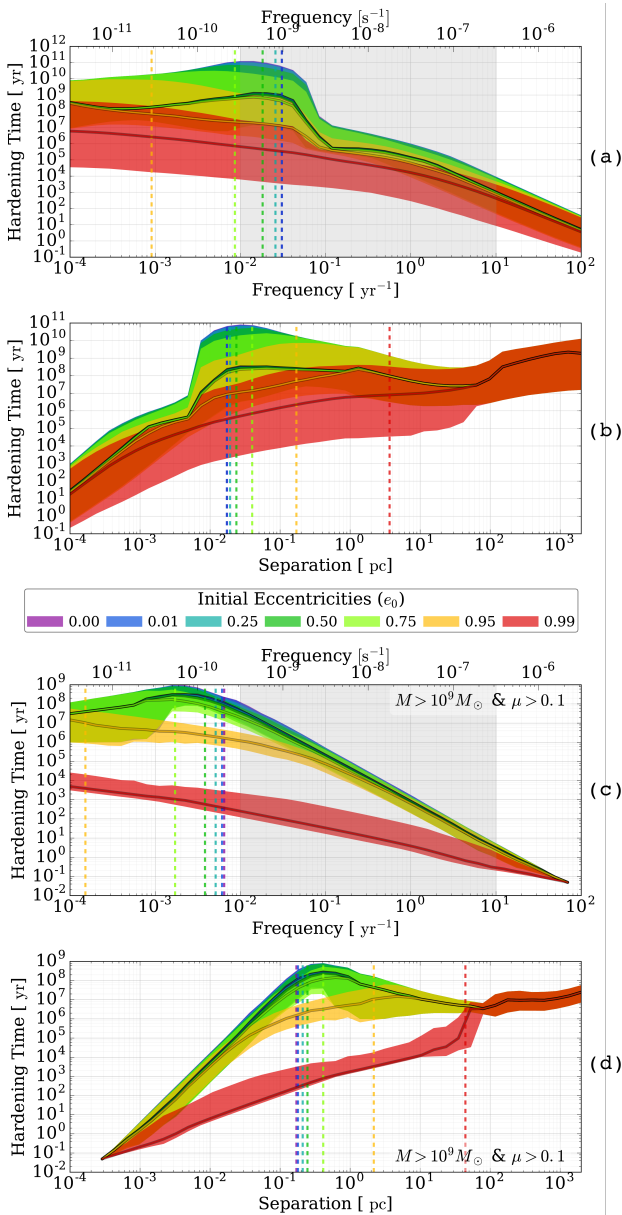


**Figure 2.** Binary hardening timescale ( $a/(da/dt)$ ) against orbital frequency (panels a & c) and binary separation (panels b & d). Note that the frequency axes show an extended range, with the PTA-sensitive band shaded in grey. The upper panels (a & b) show eccentricities for all binaries, while the lower panels (c & d) show only the *heavy & major* subset.

a few parsecs, largely circumventing the LC regime entirely. As eccentricity decreases, so does the transition radius. For lower initial eccentricities,  $e_0 \lesssim 0.75$ , the DF & LC become sub-dominant at a few times  $10^{-2}$  pc, and the overall hardening rates are hardly distinguishable between different eccentricities.

Panels (c) & (d) of Fig. 2 show the hardening time for the population of *heavy & major* binaries. While very similar to the overall population, the *heavy & major* binaries are all effectively in the GW regime at frequencies  $f \gtrsim 10^{-2} \text{ yr}^{-1}$ , i.e. the entire PTA band. In the  $e_0 = 0.0$  model, binaries in the PTA-band show a nearly perfect power-law hardening rate from GW-evolution, and eccentricities  $e_0 \lesssim 0.75$  are hardly different. In the  $e_0 = 0.95$  model, a heightened hardening rate is clearly apparent up to  $f \sim 10^{-1} \text{ yr}^{-1}$ .

The  $e_0 = 0.99$  model evolves five orders of magnitude faster than  $e_0 = 0.0$  at  $f = 10^{-2} \text{ yr}^{-1}$ , and still more than two orders faster even at  $f = 1 \text{ yr}^{-1}$ . The  $e_0 = 0.99$  model hardens drastically faster than the others both because of the strong eccentricity dependence of the GW hardening rate (Eq. 3) and because the eccentricity of the  $e_0 = 0.99$  population better retains its high values at smaller separations.

At frequencies below  $10^{-3}$ – $10^{-2} \text{ yr}^{-1}$  and lower eccentricity models ( $e_0 \lesssim 0.75$ ), the *heavy & major* population is LC-dominated, causing sharp turnovers in their hardening curves which is echoed in the resulting GWB spectra. In the population of all binaries (panel a) the transition occurs at slightly higher frequencies. The higher eccentricity models, which transition to GW domination at lower frequencies, do not show the same break in their hardening rate evolution. The resulting GWB spectra, however, still do (discussed in §3.2).

In all of our models, GW hardening is dominant to both dynamical friction and stellar scattering for the binaries which will dominate GWB production (*heavy & major* at  $f \gtrsim 10^{-2} \text{ yr}^{-1}$ ). Viscous drag, however, tends to be comparable or higher in much of the binary population. Deviations to the power-law index of hardening rates in the PTA regime are not apparent, however, because VD has a very similar radial dependence to GW emission<sup>2</sup> (see §2.2). Although the GWB spectrum is only subtly affected by VD, the presence of significant gas accretion in the PTA band is promising for observing electromagnetic counterparts to GW sources, and even multi-messenger detections with ‘deterministic’/‘continuous’ GW-sources—those MBHB resolvable above the stochastic GWB (e.g. Sesana et al. 2012; Tanaka et al. 2012; Burke-Spolaor 2013).

It should be clear from Fig. 2 that the hardening timescale is often very long ( $\tau_h \sim \tau_{\text{Hubble}}$ ) and varies significantly between binary systems. A substantial fraction of binaries, especially those with lower total mass and more extreme mass ratios, are unable to coalesce before redshift zero. The presence of significant eccentricity at sub-parsec scales can significantly decrease the hardening timescale, increasing the fraction of coalescing systems overall. The *heavy & major* subset of binaries, however, already tends to coalesce more effectively, and because this portion of the population dominates the GWB, its amplitude due to varying coalescing fractions is only subtly altered.

## 3.2 Gravitational Wave Backgrounds

### 3.2.1 The Semi-Analytic GWB

The simplest calculation of the GWB assumes that all binaries coalesce effectively, quickly, and purely due to GW emission. This leads to a purely power-law strain spectrum,  $h_{c,\text{GW}} \propto f^{-2/3}$ . Environmental hardening, however, is required for the vast majority of binaries to be able to coalesce within a Hubble time<sup>3</sup>. These additional hardening mechanisms also force binaries to pass through each frequency band faster than they otherwise would, decreasing the GW energy emitted in that band, and attenuating the GW background spectrum (e.g. Eq. 11, or Ravi et al. 2014).

Non-zero eccentricity *increases* the instantaneous GW luminosity and decreases the hardening time (Eq. 3). Also, the GW

<sup>2</sup> This is true for the inner, radiation-dominated, region of the disk where GWB-dominating binaries tend to reside.

<sup>3</sup> Even with strong external factors, hardening timescales are still often comparable to a Hubble time, and thus only a fraction of systems coalesce.

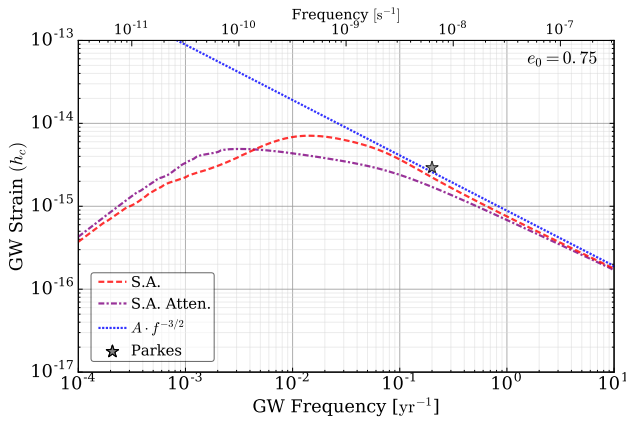


**Figure 3.** Stochastic Gravitational Wave Background calculated with the Semi-Analytic (SA) method, showing the effects of large binary eccentricities on the GWB spectrum. A purely power-law model is shown in the blue dotted line, which includes the masses and redshifts of merger events but assumes all energy is emitted in GW. The purple dot-dashed line includes the effect of attenuation from environmental hardening effects. The red dashed line shows the full SA calculation including both attenuation and the redistribution of GW energy across multiple frequencies.

emission from eccentric binaries is no longer produced monochromatically at twice the orbital frequency, but instead is redistributed, primarily from lower to higher frequencies (Eq. 6). The effects of increased attenuation and the frequency redistribution are shown separately in Fig. 3 for  $e_0 = 0.75$ . The blue, dotted line shows a power-law spectrum (i.e. GW-only); while the purple, dashed-dotted line includes attenuation from the surrounding medium (predominantly LC-scattering). The red, dashed line includes the effects of chromatic GW emission, in addition to attenuation, which shifts the spectrum to higher frequencies. This is the full, semi-analytic (SA; §2.3.1) calculation. The spectral turnover is produced by the environmental attenuation, while the frequency redistribution slightly increases the amplitude in the PTA-regime ( $f \gtrsim 10^{-2} \text{ yr}^{-1}$ ).

The GWB strain spectrum is shown for a variety of initial eccentricities in Fig. 4. Purely power-law spectra calculated assuming GW-only evolution are shown in dotted lines, while the full SA calculation is shown with dashed lines. The power-law spectra show a very slightly increasing GWB amplitude with increasing eccentricity as more binaries are able to coalesce before redshift zero. For initial eccentricities  $e_0 \lesssim 0.5$ , the GWB spectrum above frequencies  $f \gtrsim 10^{-2} \text{ yr}^{-1}$  are nearly identical. For higher initial values, the effects of non-zero eccentricity become more apparent. Overall, for all but the highest eccentricities ( $e_0 > 0.9$ ), the effect of non-circular orbits is actually to slightly increase the GWB amplitude in the PTA frequency band, because of the redistribution of GW energy to higher harmonics. Note that this is because the spectral turnover is always below the PTA-band in our spectra (also seen in, e.g., Chen et al. 2016). If galactic densities are significantly larger than those found in the Illustris simulations, the environment could continue dominating binary evolution to higher frequencies. If that were the case, the spectral turnover could be within the PTA band which would lead to chromatic GW emission *decreasing* the observable signal. In appendix §A, we include additional information on binary host-galaxy densities from Illustris.

In the highest eccentricity case ( $e_0 = 0.99$ ; red lines), binaries are still highly eccentric at separations corresponding to frequencies all the way up to  $f \sim 10 \text{ yr}^{-1}$ , and the GWB amplitude is

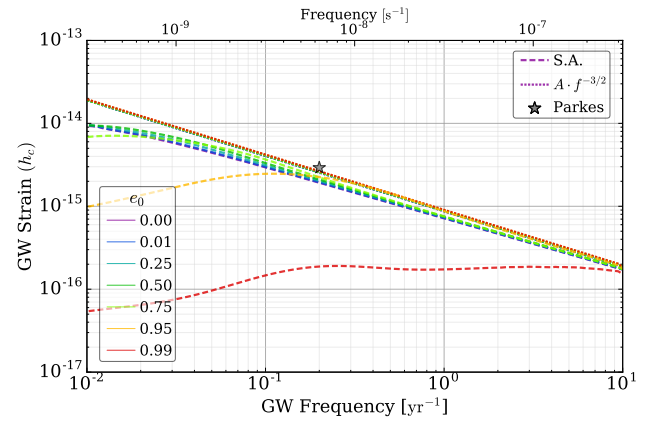


**Figure 4.** GWB strain spectrum calculate using the Semi-Analytic (SA) formalism for simulations with a range of initial eccentricities ( $e_0$ ). The dotted lines assume purely GW-driven evolution, and show amplitude increasing slightly with increasing  $e_0$ —because more systems coalesce. The dashed lines show the full SA calculation, including both attenuation and the frequency redistribution. For  $f \gtrsim 2 \times 10^{-1} \text{ yr}^{-1}$ , the GWB amplitude increases with increasing  $e_0$  until  $e_0 = 0.99$ , at which point the GWB amplitude is drastically depressed—almost completely flat—across the PTA band.

drastically diminished throughout the PTA band. While such high eccentricities may be unlikely (e.g. Armitage & Natarajan 2005; Roedig et al. 2011), having some subset of the population maintain high eccentricities into the PTA band is certainly not impossible (e.g. Rantala et al. 2016). If Kozai-Lidov-like processes from a hierarchical, third MBH were driving the eccentricity (e.g. Hoffman & Loeb 2007; Bonetti et al. 2016), or the binary were counter-rotating to the stellar core or circumbinary disk (e.g. Sesana et al. 2011; Amaro-Seoane et al. 2016), eccentricities could grow much faster than in our results. Better understanding what fraction of systems could be susceptible to these processes is an important direction of future study.

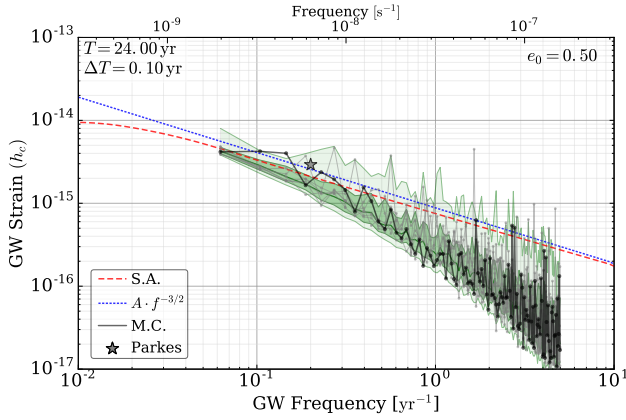
### 3.2.2 The Monte-Carlo GWB

The Monte-Carlo (MC) approach (§2.3.2) to calculating the GWB dispenses with the continuum approximation for the density of GW sources, thereby allowing for the quantization of MBHB at the same time as providing a convenient formalism for constructing an arbitrary number of realizations from the same binary population. The MC GWB is shown in Fig. 5, with seven randomly-chosen realizations plotted in gray and black. The median line and one- & two- sigma contours of 200 realizations are shown in green. For reference, the SA spectra are shown for purely power-law calculations (blue, dotted) and the full SA (red, dashed). The frequency bins correspond to Nyquist sampling at a cadence  $\Delta T = 0.1 \text{ yr}$ , and total observational-duration  $T = 24 \text{ yr}$ .

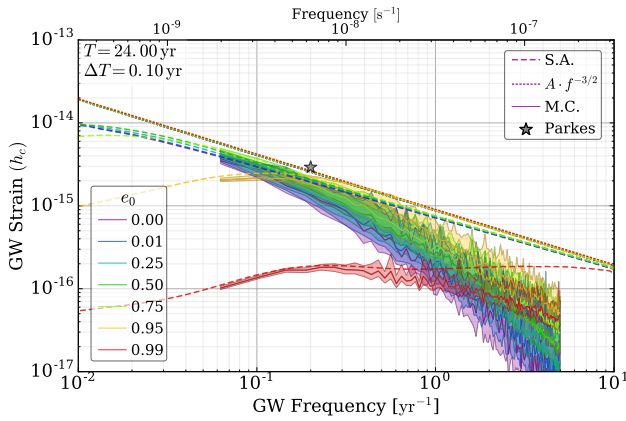
The MC GWB differs from the SA one, both in its jaggedness and also in a steeper spectrum at higher frequencies. The jaggedness is caused by varying numbers of binaries in the observer’s past light cone (Eq. 16)—especially massive ones at lower redshifts. The latter effect is due to binary quantization: at high frequencies, where the hardening time is short, there are few MBHB contributing to each frequency bin. The SA calculation, however, implicitly includes the contribution from fractional binaries, artificially inflating the GWB amplitude at high frequencies (Sesana et al. 2008).

Figure 6 shows the GWB for a variety of initial eccentricities,





**Figure 5.** GWB calculated using the Monte-Carlo (MC) method, for a simulation with initial eccentricities  $e_0 = 0.5$ . Seven different GWB realizations are shown in gray and black lines, while the median and one- & two-sigma contours are shown in green. Semi-Analytic (SA) calculations are also shown: purely power-law in blue (dotted), and full in red (dashed). The high frequency spectrum of the MC calculation is sharper than that of the SA methods due to quantization of binaries.



**Figure 6.** Monte-Carlo (MC) calculated GWB for a variety of different initial eccentricities ( $e_0$ ). Median lines and one-sigma contours are shown for the MC case, and both the full (dashed) and power-law (dotted) SA calculations are also shown. Increasing GWB amplitude with increasing eccentricity is apparent at lower frequencies ( $\sim 10^{-1} \text{ yr}^{-1}$ , until the spectrum turns over. While the spectral turnover is produced by environmental interaction, the frequency at which it occurs is increased with rising eccentricity. At higher frequencies ( $\geq 2 \times 10^{-1} \text{ yr}^{-1}$ ), as eccentricity increases, the MC results come closer and closer to the SA ones due to additional binaries at lower orbital frequencies contribute to higher *GW-frequency* bins.

with median lines and one-sigma contours for the MC calculation, along with the full and power-law SA calculations. Both the SA and MC methods show slightly increased GWB amplitudes with increasing eccentricities (except for the highest,  $e_0 = 0.99$  simulation). A more pronounced effect is that the higher the eccentricity, the closer the high-frequency portion of the MC calculation comes to the purely power-law spectra. The ratio of the MC GWB (median lines) to SA GWB is shown explicitly in Fig. C2. Higher eccentricities mean that GW energy from binaries at lower *orbital-frequencies* are deposited in higher *GW-frequency* bins. This means that overall, more binaries are contributing to each of the higher frequency bins, reducing the effect of MBHB quantization, and thus

bringing the MC results closer in line to the SA models. Finite-number effects at high frequencies are also remediated by increased numbers of coalescing systems, as is the case for very large LC refilling fractions ( $\mathcal{F}_{\text{refill}}$ ), for example, shown in Figs. C3 & C4.

### 3.3 Pulsar Timing Array Detections

To test our PTA configurations and detection statistics, we reproduce the results of Taylor et al. (2016, Fig. 2) for purely power-law GWB spectra. Our detection probabilities for each PTA are shown in Fig. C1. The left column shows expanded (+) arrays, with new pulsars added each year, while the right column shows the current array configurations. Our Detection Probabilities (DP) are close to those of Taylor et al. (2016), but not identical, likely due to differences between our noise scaling-factors  $\lambda_{\text{noise}}^4$ . For our fiducial  $A_{\text{yr}^{-1}} = 0.6 \times 10^{-15}$  (KBH-16), the individual PTA reach 95% DP after 16.8, 15.7 & 16.1 yr for the EPTA+, NANOGrav+ & PPTA+ respectively. The IPTA+ reaches the same DP in only 14.0 yr, while IPTA' cuts that down to 12.4 yr. The difference between static and expanding arrays is quite significant. In 15 years, for example, the static PTA remain at DP between 2% and 49%. Without expansion, reaching a 95% DP would take  $> 20$  yr, even with IPTA'. This highlights the importance of continued funding to telescopes like the GBT and Arecibo, not only to continue observing already-discovered pulsars, but also to continue searching for new ones.

Detection probability versus time are shown for eccentric-evolution models in Fig. 7 with expanded PTA configurations. Averages and standard deviations over 200 realizations are plotted. Ignoring the highest eccentricity case ( $e_0 = 0.99$ ), for the moment, the variation between different eccentricities is  $\leq 20\%$  in DP, and generally  $\sim 2$  yr at a fixed value. The different DP growth curves are quite similar between PTA, with DP tending to be higher for higher eccentricities between  $e_0 = 0.0$  and  $e_0 = 0.75$ . Not surprisingly, the  $e_0 = 0.99$  model is an outlier in DP as in binary evolution. In this extreme case the GWB is effectively undetectable for all PTA.

The PTA noticeably differ in their response to the  $e_0 = 0.95$  simulations which have the highest DP values for the EPTA, but the lowest for NANOGrav. In Parkes and both IPTA models, they transition from the lowest to the highest DP after  $\sim 12$ – $14$  yr. The differing responses are due to varying frequency sensitivities between arrays. Longer observing durations mean PTA are able to detect lower frequencies, and the lowest accessible frequency bins are the most sensitive (see, e.g., Moore et al. 2015). Those with the longest observing durations (Parkes and thus also IPTA) are most sensitive to the GWB spectral turnover accentuated in the high eccentricity models. As observing time increases, however, sensitivity increases at all frequencies. After a sufficient observing time, the high frequency portion of the GWB spectrum, where  $e_0 = 0.95$  is highest (see Fig. 6), gains enough leverage for  $e_0 = 0.95$  to again reach the highest DP.

In Fig. 7, the IPTA doesn't perform as well as Parkes at early times. This is due both to I) the differing noise calibrations—the IPTA's white-noise is pushed significantly higher than Parkes to match the observed upper-limits, as well as, II) the specifications for each individual PTA not quite matching those included in the

<sup>4</sup> Taylor et al. (2016) did not publish their  $\lambda_{\text{noise}}$ , but they were calculated by marginalizing against a probability distribution for  $A_{\text{yr}^{-1}}$  from Sesana (2013). We simply use a fixed value based on the GWB from our fiducial MBHB merger model,  $A_{\text{yr}^{-1}} = 0.6 \times 10^{-15}$ .

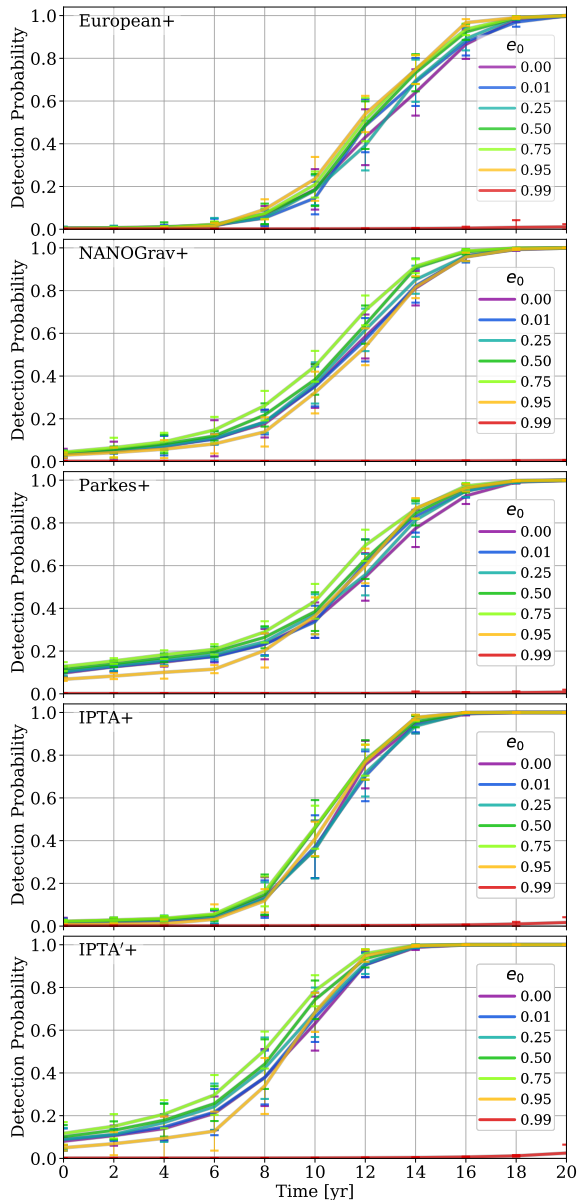


**Figure 7.** Detection Probability (DP) versus time for eccentric evolution models with different initial eccentricities ( $e_0$ , colors) and different PTA (rows). The lines and error bars are averages and standard deviations over 200 realizations. Currently ( $t = 0$ ), we find detection probabilities are below 20% for all PTA, but they reach 95% between about 12 and 18 yr. Higher eccentricities tend to be more detectable, until  $e_0 > 0.75$  where the spectral turnover takes a toll on the low-frequency GWB amplitude.

IPTA public specifications. Both of these factors motivate our inclusion of the IPTA' model, which is much more consistent with Parkes at early times. We are optimistic that future IPTA results and data releases will show even greater improvements than suggested by those of the initial IPTA results<sup>5</sup>.

<sup>5</sup> Even using the simplified and already preprocessed public PTA data, and our simplified statistical analysis, the challenge of combining and analyzing the disparate PTA data is quite clear. Calling the task 'non-trivial' is surely a significant understatement, and thus entirely consistent with its usage in astrophysical literature.

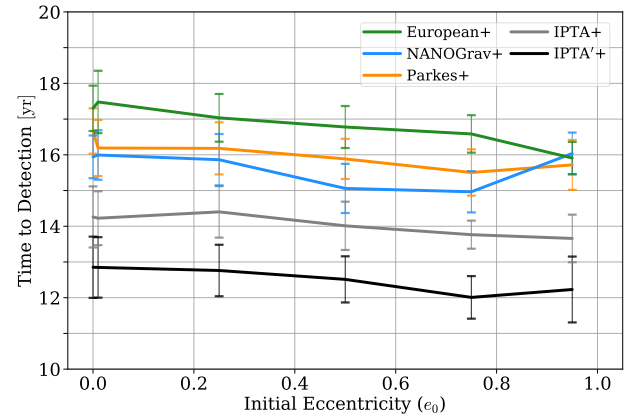


**Figure 8.** Time to reach a 95% DP versus initial eccentricity ( $e_0$ ) of MBH binaries. Each (expanded, '+') PTA is shown with the average and standard deviation of 200 realizations. The public IPTA+ specification shows a noticeable improvement over the individual PTA, with detection likely in roughly 14 yr. The more optimistic IPTA' model improves that further to 12–13 yr.

Figure 8 shows times to reach 95% DP versus initial eccentricity for each PTA. Overall, time to detection tends to improve slightly with increasing eccentricity as it increases the GWB amplitude in the mid-to-upper PTA band. Differences between eccentricities, however, tend to be smaller than the variance between realizations. For very high eccentricities,  $e_0 > 0.75$ , the time to detection again increases as the GWB spectral turnover becomes 'visible' to PTA, and the signal is diminished. While the  $e_0 = 0.99$  models never reach 95% DP in our results, additional simulations suggest that observational cadences on the order of a day would be required to make detections plausible for this most extreme eccentricity model. Even in the highest eccentricity model with  $e_0 = 0.99$ , detection prospects for individual, deterministic sources may not be affected quite as strongly. We are currently exploring single source predictions from our models, to be presented in a future study.

Detection probability versus time for *circular* evolution models with a variety of loss-cone refilling parameters ( $\mathcal{F}_{\text{refill}}$ ) are shown in Fig. 9. Recall that a low, 'steady-state LC' corresponds to  $\mathcal{F}_{\text{refill}} = 0.0$ , and a highly effective, 'full LC' to  $\mathcal{F}_{\text{refill}} = 1.0$ . Overall a similar range of durations are required for comparable DP, but the circular models are systematically harder to detect, taking roughly 2 years longer. This is not surprising as the eccentric models assume a full LC, and increasing eccentricity tends to further enhance the GWB amplitude in the PTA band. In general, higher  $\mathcal{F}_{\text{refill}}$  lead to higher DP after a fixed time. The circular, full LC, shows a slight decrease in DP for the European, NANOGrav, and Parkes PTA as the attenuation and spectral turnover from stellar scattering take effect, analogous to the highest eccentricities (see, e.g., Fig. C3). For both IPTA models, sensitivity continues to improve between the  $\mathcal{F}_{\text{refill}} = 0.8$  and  $\mathcal{F}_{\text{refill}} = 1.0$ , suggesting that their high-frequency sensitivities are able to win out.

Figure 10 summarizes the circular-evolution times to detection for each PTA versus  $\mathcal{F}_{\text{refill}}$  (solid lines). For the individual PTA, the steady-state loss-cone model implies an additional 2 years of required observations compared to a full LC. Overall, all three individual PTA reach 95% DP within one year of each other. The IPTA & IPTA' reach the same probability 2 & 3 yr earlier, except for  $\mathcal{F}_{\text{refill}} = 1.0$ , where the IPTA & IPTA' reach 95% DP 3 & 5 yr faster respectively. For highly effective LC, like high eccentricities,

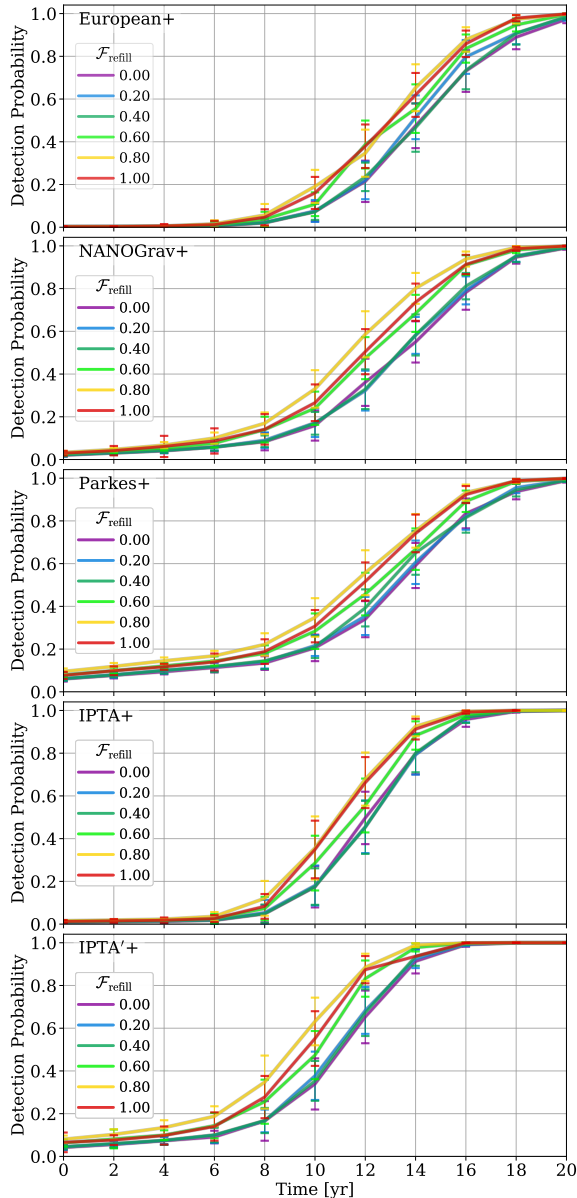


**Figure 9.** DP versus time for circular evolution models with different LC efficiencies ( $\mathcal{F}_{\text{refill}}$ , colors) and different expanded PTA (rows). These growth curves behave very similarly to those of the eccentric models, but generally take  $\sim 2$  yr longer to reach the same DP. There is also a stronger trend across  $\mathcal{F}_{\text{refill}}$  compared to  $e_0$ , with  $\mathcal{F}_{\text{refill}} = 0.00$  reaching the same DP  $\sim 2$  yr slower than for  $\mathcal{F}_{\text{refill}} \sim 0.8-1.0$ .

more MBHB contribute to the GWB signal at higher frequencies, where the IPTA models have ever larger advantages.

Overplotted on Fig. 10 are the eccentric-evolution times to detection (dashed lines, upper x-axis) for comparison. Imagining a hybrid merger model which includes both eccentric evolution (assuming  $e \lesssim 0.95$ ) and a varying scattering efficiency, a steady-state LC with zero eccentricity would be the hardest to detect, requiring  $\sim 16$  &  $15$  yr to reach 95% DP for the IPTA & IPTA'. The easiest detection case would be a full or nearly full LC ( $\mathcal{F}_{\text{refill}} \approx 1.0$ ), with moderate-to-high eccentricities ( $0.7 \lesssim e \lesssim 0.9$ ), which would take  $\sim 13$  &  $11$  yr.

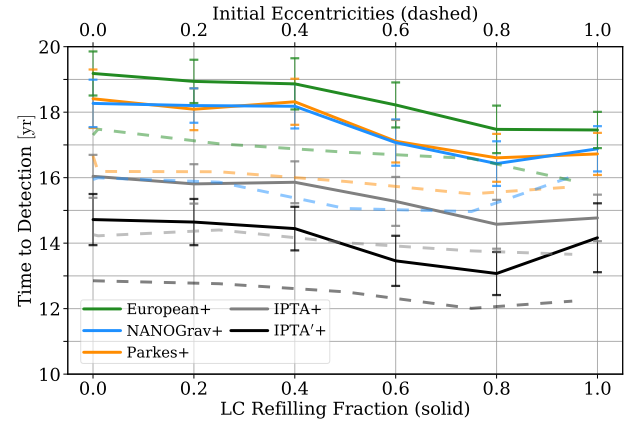


**Figure 10.** Time to reach a 95% DP versus LC refilling fraction ( $\mathcal{F}_{\text{refill}}$ ; solid lines) for circular binary-evolution models. The times to detection for varying eccentricity models (from Fig. 8) are overplotted with faint dashed lines for comparison. Averages and standard deviations over 200 realizations are shown for each expanded PTA. Varying  $\mathcal{F}_{\text{refill}}$  has a pronounced effect on detection times, with more effective scattering (larger  $\mathcal{F}_{\text{refill}}$ ) models taking less time to observe. The difference between a full loss-cone and a steady-state one amounts to 3–5 additional years of observations. Because the eccentric evolution models assume a full loss-cone, the  $\mathcal{F}_{\text{refill}} < 1.0$  models tend to take longer to be detected.

## 4 CONCLUSIONS

This paper has focused on plausible detections of a stochastic Gravitational Wave Background (GWB) using Pulsar Timing Arrays (PTA). We have expanded on the Massive Black-Hole (MBH) merger models presented in Kelley et al. (2016) based on the Illustris simulations. We have added a model for eccentric binary evolution assuming ‘full’ Loss-Cone (LC) stellar scattering, in addition to our existing prescriptions for dynamical friction, stellar scattering with a variety of LC efficiencies ( $\mathcal{F}_{\text{refill}}$ ), viscous drag from a circumbinary disk, and Gravitational Wave (GW) emission. We have run sets of simulations with a variety of LC efficiencies and initial (at the start of stellar scattering) eccentricities. The MBH binary evolution produced by our models is explored along with Monte-Carlo (MC) realizations of the resulting stochastic GW Background (GWB) spectra. Using parametrized models of currently operational PTA, and their future expansion, we calculate realistic prospects for detections of the GWB.

The presence of non-zero eccentricity causes two distinct effects to MBH Binary (MBHB) evolution and their GW spectra. First, increased eccentricity causes faster GW-hardening and thus more binary coalescence, but there is additional attenuation of the GWB spectrum and a stronger spectral turnover at low frequencies. Second, while circular binaries emit GW at only twice the orbital frequency (the  $n = 2$  harmonic), eccentric binaries also emit at all higher harmonics (and the  $n = 1$ ). The total GW energy released remains the same, but the overall effect is to move GW energy from lower to higher frequencies (Fig. 3).

GWB spectra constructed using a Semi-Analytic (SA) calculation (Fig. 4) show that the amplitude ( $A_{\text{yr}^{-1}}$ ) of the GWB near the middle of the PTA band ( $f \sim 1 \text{ yr}^{-1}$ ) tends to increase with increasing eccentricity up to  $e_0 = 0.95$ . This is due primarily to the first eccentric effect: with hardening more effective, the number of binaries coalescing by redshift zero increases. At lower frequencies, environmental effects—specifically stellar scattering—produce a strong turnover in the GWB spectrum. Even moderate

eccentricities begin to increase the frequency at which this turnover occurs because of the second eccentric effect. Unless the population of binaries dominating the GWB have very high eccentricities ( $e \gtrsim 0.8$ ), the spectral turnover remains below the PTA sensitive band ( $f \lesssim 0.02 \text{ yr}^{-1}$ ).

The location of the spectral turnover in our models differs from those predicted by Ravi et al. (2014) who see the turnover at frequencies as high as  $f \sim 10^{-1} \text{ yr}^{-1}$ . The location of the turnover depends on the strength of environmental factors, and thus galactic density profiles. If the stellar densities of massive-MBHB host-galaxies are higher than predicted by Illustris, the turnover could occur at PTA-observable frequencies, regardless of (or exaggerated by) eccentricity distribution. If the turnover does exist in the current PTA band, it could hurt detection prospects. At the same time, observations of such a turnover would be uniquely indicative of environmental interactions, while observations of the GWB amplitude overall are highly degenerate between cosmological factors (i.e. the rate of binary formation) and environmental factors (determining the rate of binary coalescence). Currently PTA upper limits of the GWB are still entirely consistent with our results, and thus are unable to constrain or select between them.

GWB spectra constructed using the MC calculation (Fig. 6), which should resemble real signals, tend to have much steeper strain spectra than  $-2/3$  at current PTA frequencies ( $f \gtrsim 0.1 \text{ yr}^{-1}$ ). This is because the number of binaries in each frequency bin becomes small, and binary quantization must be taken into account. MC realizations reveal an interesting corollary to the redistribution of GW energy: with non-zero eccentricity, a larger number of binaries at lower *orbital-frequencies* contribute to the GWB signal at higher *observed-frequency* bins. This softens the effect of binary quantization and the GWB spectra tend to come closer and closer to a  $-2/3$  spectral index with increasing eccentricity (Fig. C2)—thus producing higher  $A_{\text{yr}^{-1}}$ . For example, the  $e_0 = 0.5$  &  $e_0 = 0.95$  models have  $A_{\text{yr}^{-1}}$ , 2 & 3 times larger than that of the  $e_0 = 0.0$  model.

To calculate realistic detection statistics, we use parametrized version of each operational PTA: the European (EPTA), NANOGrav, Parkes (PPTA), and International (IPTA; a joint effort of the individual three). We also include an optimistic combination of the individual groups, IPTA', which may represent a more realistic model for future IPTA results. Overall, each PTA behaves comparably, but the IPTA and especially IPTA' reach higher Detection Probabilities (DP) on shorter timescales. Using the time to 95% DP as a metric, we find that the IPTA will likely make a detection within 13–16 years, or 11–15 for the IPTA' model. The individual PTA generally require 2–3 additional years of observations to reach the same DP. In some models where the low-frequency component of the GWB is significantly attenuated (by especially high eccentricities, or strong environmental interactions) the IPTA models can take 5–6 years less time, due to heightened high-frequency sensitivity.

Increased eccentricity tends to increase the GWB amplitude, and thus detection prospects. In the most extreme  $e_0 = 0.99$  model, however, the signal is so drastically diminished that detections seem unlikely within 20 years. While eccentricities as high as 0.99 may not be representative of the overall population of binaries, mechanisms (e.g. counter-rotating stars/gas, Khan et al. 2011; Amaro-Seoane et al. 2016, or three-body resonances) which can preferentially drive more massive systems to higher eccentricities should be further studied. Varying the eccentricity distribution of binaries has a strong effect on the strain spectral-index of the GWB at high frequencies ( $f \gtrsim 1 \text{ yr}^{-1}$ ). While PTA are less sensitive at higher frequencies, eventual observations with high signal-to-

noise could be used to constrain the underlying binary eccentricity distribution. The true eccentricity distribution will also affect the prospects for observations of individual, resolvable binaries ('deterministic'/'continuous' sources)—a study of which is currently in progress.

Low frequency sensitivity is established by long observing baselines, but we find that including short cadence observations to maintain or improve high frequency sensitivity can make a noticeable difference in detection prospects for more extreme hardening/eccentricity models. Regardless of cadence, we find that the continued addition of pulsars monitored by PTA is *essential* for a detection to be made within the next 20 years. Across a wide range of specific configurations, and even with pessimistic model parameters, if PTA continue to expand as they are, GWB detections are highly likely within 10–15 years.

## ACKNOWLEDGMENTS

We are grateful to both Pablo Rosado and Stephen Taylor who were both extremely helpful in clarifying details of the PTA detection statistics, and providing insight throughout the process of this project.

This research made use of Astropy, a community-developed core Python package for Astronomy (Astropy Collaboration et al. 2013), in addition to SciPy (Jones et al. 01), ipython (Prez & Granger 2007), NumPy (Van Der Walt et al. 2011). All figures were generated using matplotlib (Hunter 2007).

## REFERENCES

- Amaro-Seoane P., Sesana A., Hoffman L., Benacquista M., Eichhorn C., Makino J., Spurzem R., 2010, *Mon. Not. R. Astron. Soc.*, **402**, 2308  
Amaro-Seoane P., Maureira-Fredes C., Dotti M., Colpi M., 2016, *Astron. Astrophys.*, **591**, A114  
Armitage P. J., Natarajan P., 2005, *Astrophys. J.*, **634**, 921  
Arzoumanian Z., et al., 2015, preprint, ([arXiv:1508.03024](https://arxiv.org/abs/1508.03024))  
Astropy Collaboration et al., 2013, *Astron. Astrophys.*, **558**, A33  
Begelman M. C., Blandford R. D., Rees M. J., 1980, *Nature*, **287**, 307  
Binney J., Tremaine S., 1987, *Galactic dynamics*. Princeton University Press  
Bonetti M., Haardt F., Sesana A., Barausse E., 2016, *Mon. Not. R. Astron. Soc.*, **461**, 4419  
Burke-Spolaor S., 2013, *Classical and Quantum Gravity*, **30**, 224013  
Caballero R. N., et al., 2016, *Mon. Not. R. Astron. Soc.*, **457**, 4421  
Chandrasekhar S., 1943, *Astrophys. J.*, **97**, 255  
Chen S., Sesana A., Del Pozzo W., 2016, preprint, ([arXiv:1612.00455](https://arxiv.org/abs/1612.00455))  
Colpi M., Mayer L., Governato F., 1999, *Astrophys. J.*, **525**, 720  
Cuadra J., Armitage P. J., Alexander R. D., Begelman M. C., 2009, *Mon. Not. R. Astron. Soc.*, **393**, 1423  
Dehnen W., 1993, *Mon. Not. R. Astron. Soc.*, **265**, 250  
Desvignes G., et al., 2016, *Mon. Not. R. Astron. Soc.*, **458**, 3341  
Detweiler S., 1979, *Astrophys. J.*, **234**, 1100  
Enoki M., Nagashima M., 2007, *Progress of Theoretical Physics*, **117**, 241  
Faber S. M., et al., 1997, *Astron. J.*, **114**, 1771  
Finn L. S., Larson S. L., Romano J. D., 2009, *Phys. Rev. D*, **79**, 062003  
Foster R. S., Backer D. C., 1990, *Astrophys. J.*, **361**, 300  
Genel S., et al., 2014, *Mon. Not. R. Astron. Soc.*, **445**, 175  
Haiman Z., Kocsis B., Menou K., 2009, *Astrophys. J.*, **700**, 1952  
Hellings R. W., Downs G. S., 1983, *Astrophys. J. Lett.*, **265**, L39  
Hernquist L., 1990, *Astrophys. J.*, **356**, 359  
Hobbs G., et al., 2010, *Classical and Quantum Gravity*, **27**, 084013  
Hoffman L., Loeb A., 2007, *Mon. Not. R. Astron. Soc.*, **377**, 957  
Hogg D. W., 1999, *ArXiv Astrophysics e-prints*,

- Hunter J. D., 2007, *Computing In Science & Engineering*, 9, 90
- Jaffe A. H., Backer D. C., 2003, *The Astrophysical Journal*, 583, 616
- Jones E., Oliphant T., Peterson P., et al., 2001–, SciPy: Open source scientific tools for Python, [Link](#)
- Kelley L. Z., Blecha L., Hernquist L., 2016, preprint, ([arXiv:1606.01900](#))
- Khan F. M., Just A., Merritt D., 2011, *Astrophys. J.*, 732, 89
- Kocsis B., Sesana A., 2011, *Mon. Not. R. Astron. Soc.*, 411, 1467
- Kramer M., Champion D. J., 2013, *Classical and Quantum Gravity*, 30, 224009
- Lauer T. R., et al., 2007, *Astrophys. J.*, 664, 226
- Lentati L., et al., 2015, *Mon. Not. R. Astron. Soc.*, 453, 2576
- Lentati L., et al., 2016, *Mon. Not. R. Astron. Soc.*, 458, 2161
- Magorrian J., Tremaine S., 1999, *Mon. Not. R. Astron. Soc.*, 309, 447
- Manchester R. N., et al., 2013, *PASA*, 30, e017
- McLaughlin M. A., 2013, *Classical and Quantum Gravity*, 30, 224008
- McWilliams S. T., Ostriker J. P., Pretorius F., 2014, *Astrophys. J.*, 789, 156
- Milosavljević M., Merritt D., 2003, *Astrophys. J.*, 596, 860
- Moore C. J., Taylor S. R., Gair J. R., 2015, *Classical and Quantum Gravity*, 32, 055004
- Nelson D., et al., 2015, *Astronomy and Computing*, 13, 12
- Peters P. C., 1964, *Physical Review*, 136, 1224
- Peters P. C., Mathews J., 1963, *Physical Review*, 131, 435
- Phinney E. S., 2001, ArXiv Astrophysics e-prints,
- Prez F., Granger B., 2007, *Computing in Science Engineering*, 9, 21
- Quinlan G. D., 1996, *New Astron.*, 1, 35
- Quinlan G. D., Hernquist L., 1997, *New Astron.*, 2, 533
- Rajagopal M., Romani R., 1994, arXiv preprint astro-ph/9412038
- Rajagopal M., Romani R. W., 1995, *Astrophys. J.*, 446, 543
- Rantala A., Pihajoki P., Johansson P. H., Naab T., Lahén N., Sawala T., 2016, preprint, ([arXiv:1611.07028](#))
- Rasskazov A., Merritt D., 2016, preprint, ([arXiv:1606.07484](#))
- Ravi V., Wyithe J. S. B., Shannon R. M., Hobbs G., Manchester R. N., 2014, *Mon. Not. R. Astron. Soc.*, 442, 56
- Reardon D. J., et al., 2016, *Mon. Not. R. Astron. Soc.*, 455, 1751
- Roebber E., Holder G., Holz D. E., Warren M., 2016, *Astrophys. J.*, 819, 163
- Roedig C., Dotti M., Sesana A., Cuadra J., Colpi M., 2011, *Mon. Not. R. Astron. Soc.*, 415, 3033
- Romani R. W., Taylor J. H., 1983, *Astrophys. J. Lett.*, 265, L35
- Rosado P. A., Sesana A., Gair J., 2015, *Mon. Not. R. Astron. Soc.*, 451, 2417
- Sazhin M. V., 1978, *Soviet Astronomy*, 22, 36
- Sesana A., 2010, *Astrophys. J.*, 719, 851
- Sesana A., 2013, *Mon. Not. R. Astron. Soc.*, 433, L1
- Sesana A., Haardt F., Madau P., 2006, *Astrophys. J.*, 651, 392
- Sesana A., Vecchio A., Colacino C. N., 2008, *Mon. Not. R. Astron. Soc.*, 390, 192
- Sesana A., Gualandris A., Dotti M., 2011, *Mon. Not. R. Astron. Soc.*, 415, L35
- Sesana A., Roedig C., Reynolds M. T., Dotti M., 2012, *Mon. Not. R. Astron. Soc.*, 420, 860
- Sesana A., Shankar F., Bernardi M., Sheth R. K., 2016, preprint, ([arXiv:1603.09348](#))
- Shannon R. M., et al., 2015, *Science*, 349, 1522
- Shapiro S. L., Teukolsky S. A., 1986, *Black Holes, White Dwarfs and Neutron Stars: The Physics of Compact Objects*
- Sijacki D., Vogelsberger M., Genel S., Springel V., Torrey P., Snyder G. F., Nelson D., Hernquist L., 2015, *Mon. Not. R. Astron. Soc.*, 452, 575
- Snyder G. F., et al., 2015, *Mon. Not. R. Astron. Soc.*, 454, 1886
- Springel V., 2010, *Mon. Not. R. Astron. Soc.*, 401, 791
- Tanaka T., Menou K., Haiman Z., 2012, *Mon. Not. R. Astron. Soc.*, 420, 705
- Taylor S. R., Vallisneri M., Ellis J. A., Mingarelli C. M. F., Lazio T. J. W., van Haasteren R., 2016, *Astrophys. J. Lett.*, 819, L6
- The NANOGrav Collaboration et al., 2015, *Astrophys. J.*, 813, 65
- Torrey P., Vogelsberger M., Genel S., Sijacki D., Springel V., Hernquist L., 2014, *Mon. Not. R. Astron. Soc.*, 438, 1985
- Van Der Walt S., Colbert S. C., Varoquaux G., 2011, preprint, ([arXiv:1102.1523](#))
- Verbiest J. P. W., et al., 2016, preprint, ([arXiv:1602.03640](#))
- Vigeland S. J., Siemens X., 2016, *Phys. Rev. D*, 94, 123003
- Vogelsberger M., Genel S., Sijacki D., Torrey P., Springel V., Hernquist L., 2013, *Mon. Not. R. Astron. Soc.*, 436, 3031
- Vogelsberger M., et al., 2014a, *Mon. Not. R. Astron. Soc.*, 444, 1518
- Vogelsberger M., et al., 2014b, *Nature*, 509, 177
- Volonteri M., Madau P., Haardt F., 2003, *Astrophys. J.*, 593, 661
- Wyithe J. S. B., Loeb A., 2003, *Astrophys. J.*, 590, 691
- de Vaucouleurs G., 1948, *Annales d’Astrophysique*, 11, 247

## APPENDIX A: HOST-GALAXY DENSITIES IN ILLUSTRIS

The point at which two MBH come within a smoothing length of one another is identified in Illustris, and density profiles are calculated for the host galaxy at that time. The profiles are used to calculate the environmental hardening rates which then determine the GWB spectra. In particular, the stellar densities strongly affect the location of the spectral turnover through stellar scattering. Because the location of the spectral turnover is especially important for future detections of the GWB, we provide some additional details on the stellar environments here.

To calculate density profiles, we average the density of each particle type (star, dark matter, and gas) in radial bins. Because Illustris is only able to resolve down to 10s–100s of parsec scales, we extrapolate to smaller radii with power-law fits to the eight inner-most bins<sup>1</sup>. Fig. A1 shows the distribution of stellar densities at 10 pc (interpolated or extrapolated as needed) in the upper-panel<sup>2</sup>, and power-law indices in the lower-panel. The overall population of binaries are shown in grey (dashed), in addition to the *heavy* ( $M > 10^9 M_{\odot}$ ) subset in blue, and *heavy & major* ( $\mu > 0.1$ ) mass-ratio subset in red. There is a roughly 100 times increase in typical stellar densities between *heavy* systems and overall host-galaxies, but no noticeable change when further selecting by mass-ratio. While the *heavy* subset constitutes less than 10% of systems, they contribute ~90% of the GWB amplitude (see, KBH-16).

The median power-law index for the inner stellar density profiles is  $\sim -0.4$ . For comparison, at small radii an Hernquist (1990) profile corresponds to  $-1$ , and  $-1.5$  produces a surface-density distribution that resembles a de Vaucouleurs (1948) profile (Dehnen 1993). At the same time, many massive galaxies (comparable to our host galaxies) have flattened ‘cores’ in their stellar density profiles (e.g. Faber et al. 1997; Lauer et al. 2007) and it has long been proposed that these cores could be explained by dynamical scouring from MBH binaries (e.g. Quinlan & Hernquist 1997; Volonteri et al. 2003). Both computationally and observationally, inner density profiles in the ‘hard’ binary regime (typically  $r \lesssim 10$  pc) are very difficult to resolve. It is thus unclear how accurate these profiles are. While they may be realistic models, some of the flattening in the inner regions may be due in part to numerical effects (e.g. gravitational softening in the force calculations) or the known, over-inflated radii of some galaxies in Illustris (Snyder et al. 2015; Kelley et al. 2016).

<sup>1</sup> Restricted to those which contain at least four particles each.

<sup>2</sup> We choose 10 pc as it is near typical spheres of influence ( $\mathcal{R}_{\text{infl}}$ ) & hardening radii ( $R_h$ ) for our systems, observational resolution-limits for nearby galaxies, and usually just beneath Illustris resolution-limits.

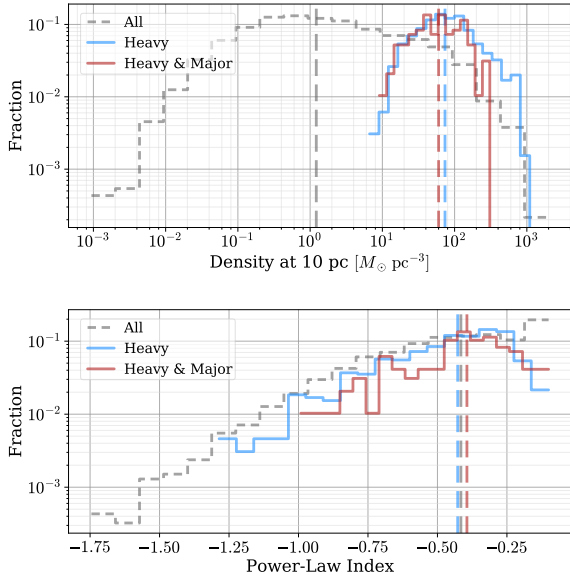


**Figure A1.** Upper-panel: distribution of stellar densities at 10 pc for Illustris galaxies hosting MBH binaries. For galaxies in which 10 pc is unresolved, the density is calculated from power-law fits to the inner-most (resolved) regions. The dashed grey lines show the entire population of binary host galaxies, while the blue lines show hosts of *heavy* ( $M > 10^9 M_\odot$ ) binaries, and red the *heavy and major* ( $\mu > 0.1$ ) binaries. Each population is plotted fractionally, but note that *heavy* binaries constitute  $\sim 7\%$  and *heavy & major*  $\sim 1\%$  of all binaries respectively. Vertical lines indicate the median value of each subset.

## APPENDIX B: ADDITIONAL EQUATIONS

The GW frequency distribution function can be expressed as (Peters & Mathews 1963, Eq. 20),

$$g(n, e) \equiv \frac{n^4}{32} \left( [G_1]^2 + [1 - e^2][G_2]^2 + \frac{4}{3n^2} [J_n(ne)]^2 \right),$$

$$G_1(n, e) \equiv J_{n-2}(ne) - 2eJ_{n-1}(ne) + \frac{2}{n}J_n(ne) + 2eJ_{n+1}(ne) - J_{n+2}(ne),$$

$$G_2(n, e) \equiv J_{n-2}(ne) - 2eJ_n(ne) + J_{n+2}(ne).$$

(B1)

Here  $J_n(x)$  is the  $n$ 'th Bessel Function of the first kind. The sum of all harmonics,  $\sum_{n=1}^{\infty} g(n, e) = F(e)$ , where  $F(e)$  is defined in Eq. 4.

The observed, characteristic strain from a set of individual sources is (e.g. Rosado et al. 2015, Eq. 8),

$$h_c^2 = \sum_i h_{s,i}^2 \frac{f_i}{\Delta f} \approx \sum_i h_{s,i}^2 f_i T, \quad (\text{B2})$$

where the second equality assumes that frequency bins are determined by the resolution corresponding to a total observational duration  $T$ .

The cosmological evolution function is (Hogg 1999, Eq. 14),

$$E(z) \equiv \sqrt{\Omega_M(1+z)^3 + \Omega_k(1+z)^2 + \Omega_\Lambda}, \quad (\text{B3})$$

for  $z$  the redshift, and  $\Omega_M$ ,  $\Omega_k$  &  $\Omega_\Lambda$  the density parameters for matter, curvature and dark-energy.

## B1 Detection Formalism

In what follows, the GWB signal is characterized by a Spectral Energy Density (SED),

$$S_h = \frac{h_c^2}{12\pi^2 f^3}, \quad (\text{B4})$$

and the prediction/model SED is denoted as  $S_{h0}$ . In all of our calculations, we use a purely power-law GWB spectrum for  $S_{h0}$  with an amplitude of  $A_{\gamma^{-1}} = 10^{-16}$ . Each pulsar  $i$  is characterized by a noise SED  $P_i$  (Eq. 18).

PTA detection statistics typically rely on cross-correlations between signals using an ‘overlap reduction function’ (the Hellings & Downs 1983, curve),

$$\Gamma_{ij} = \frac{3}{2}\gamma_{ij} \ln(\gamma_{ij}) - \frac{1}{4}\gamma_{ij} + \frac{1}{2} + \frac{1}{2}\delta_{ij} \quad (\text{B5})$$

where,

$$\gamma_{ij} = \frac{1}{2} [1 - \cos(\theta_{ij})], \quad (\text{B6})$$

for an angle between pulsars  $i$  and  $j$ ,  $\theta_{ij}$ .

We employ the ‘B-Statistic’ from Rosado et al. (2015), constructed by maximizing the statistic’s SNR—defined as the expectation value of the statistic in the presence of a signal,

$$\mu_{B1} = 2 \sum_k \sum_{ij} \frac{\Gamma_{ij}^2 S_h S_{h0}}{(P_i + S_{h0})(P_j + S_{h0}) + \Gamma_{ij}^2 S_{h0}^2}, \quad (\text{B7})$$

divided by the variance of the statistic also in the presence of a signal,

$$\sigma_{B1}^2 = 2 \sum_k \sum_{ij} \frac{\Gamma_{ij}^2 S_{h0}^2 [(P_i + S_h)(P_j + S_h) + \Gamma_{ij}^2 S_h^2]}{[(P_i + S_{h0})(P_j + S_{h0}) + \Gamma_{ij}^2 S_{h0}^2]^2}, \quad (\text{B8})$$

i.e.  $S/N_B \equiv \mu_{B1}/\sigma_{B1}$ , as apposed to the variance in the *absence* of a signal,

$$\sigma_{B0}^2 = 2 \sum_k \sum_{ij} \frac{\Gamma_{ij}^2 S_{h0}^2 P_i P_j}{[(P_i + S_{h0})(P_j + S_{h0}) + \Gamma_{ij}^2 S_{h0}^2]^2}. \quad (\text{B9})$$

The SNR can then be expressed as,

$$S/N^2 = S/N_B^2 = 2 \sum_k \sum_{ij} \frac{\Gamma_{ij}^2 S_h^2}{P_i P_j + S_h (P_i + P_j) + S_h^2 (1 + \Gamma_{ij}^2)}, \quad (\text{B10})$$

which is only meaningful compared to the threshold-SNR for a particular false-alarm probability ( $\alpha_0$ ) and DP-threshold ( $\gamma_0$ ),

$$S/N_B^T = \sqrt{2} \left[ \frac{\sigma_0}{\sigma_1} \text{erfc}^{-1}(2\alpha_0) - \text{erfc}^{-1}(2\gamma_0) \right]. \quad (\text{B11})$$

The SNR can be circumvented altogether by considering the measured DP,

$$\gamma_B = \frac{1}{2} \text{erfc} \left( \frac{\sqrt{2} \sigma_0 \text{erfc}^{-1}(2\alpha_0) - \mu_1}{\sqrt{2} \sigma_1} \right), \quad (\text{B12})$$

which is the primary metric we use throughout our analysis of PTA detections.

## APPENDIX C: ADDITIONAL FIGURES

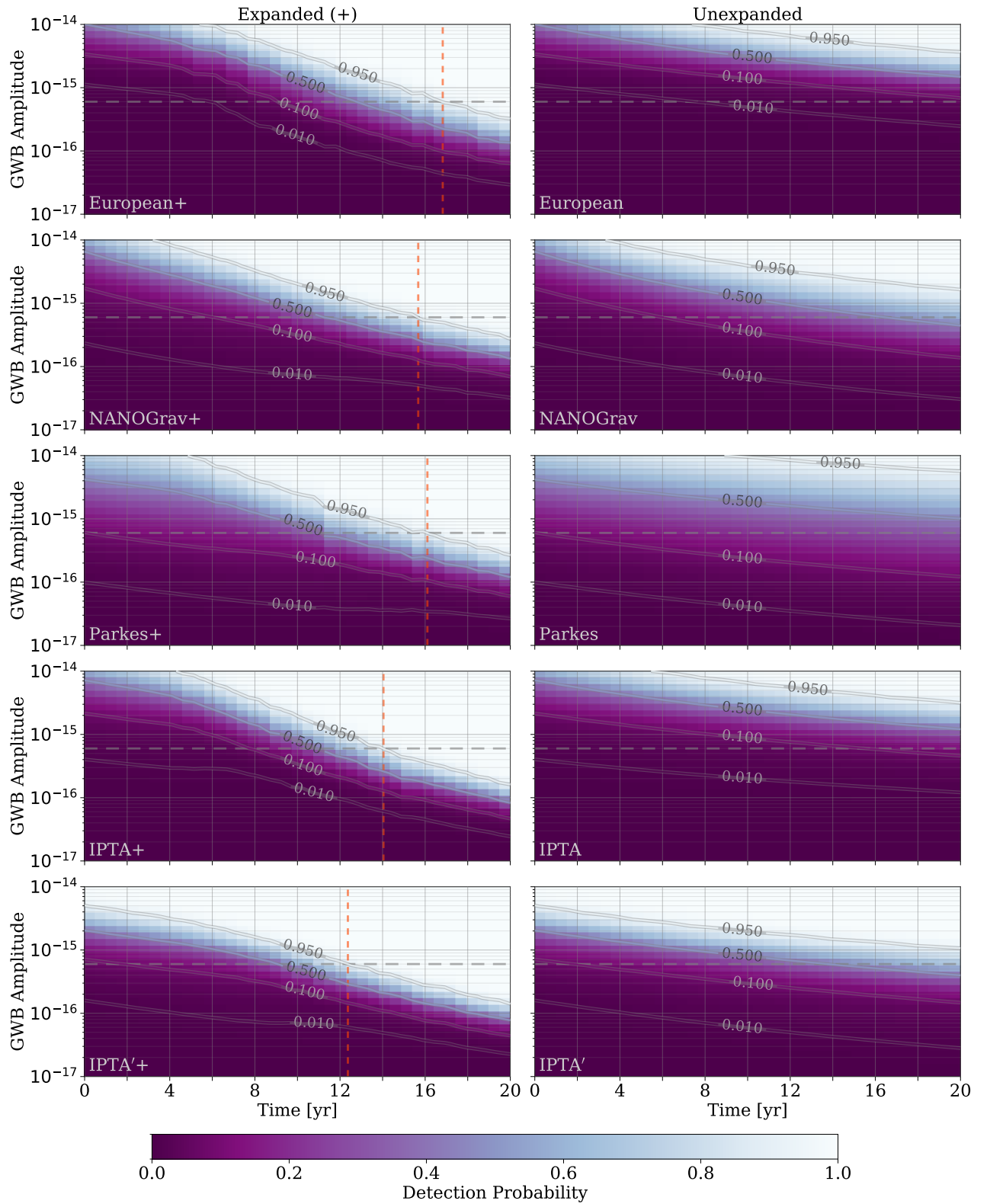


**Figure C1.** Detection Probability (DP) for purely power-law GWB spectra exploring different intrinsic GWB amplitudes over different observation durations (after 2017/01/01). The left column shows the expanded (+) configurations where new pulsars are added each year, while the right column shows the static configurations with only the current number of pulsars. The IPTA is the official specification for the combined, international pulsar timing array, while the IPTA' is a more optimistic, manual combination of the specifications for each of the three individual PTA (see §2.4). The horizontal, dashed grey lines show the GWB amplitude from our fiducial models:  $A_{yr-1} = 0.6 \times 10^{-15}$ , and the vertical, dashed orange lines show the time at which each configuration reaches  $DP = 95\%$  for the fiducial amplitude. For the IPTA+, the time to the fiducial amplitude is 14.0 yr.

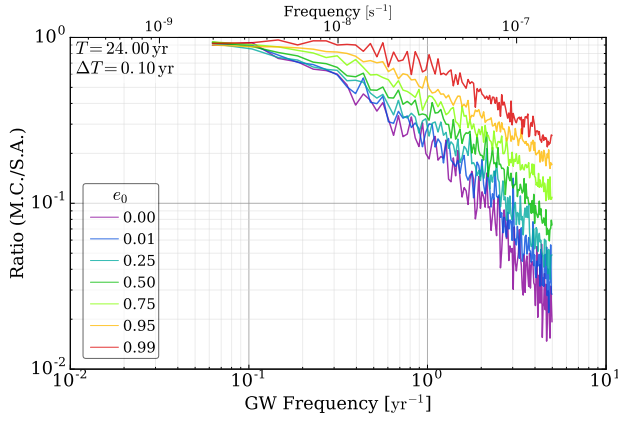


**Figure C2.** Ratio of the (median) MC-calculated GWB to that of the SA calculation. Binaries at higher eccentricities contribute more GW energy to higher-harmonics above their orbital frequency. This causes the number of sources contributing at higher-frequencies to increase with increasing eccentricity, decreasing the effects of MBHB quantization.

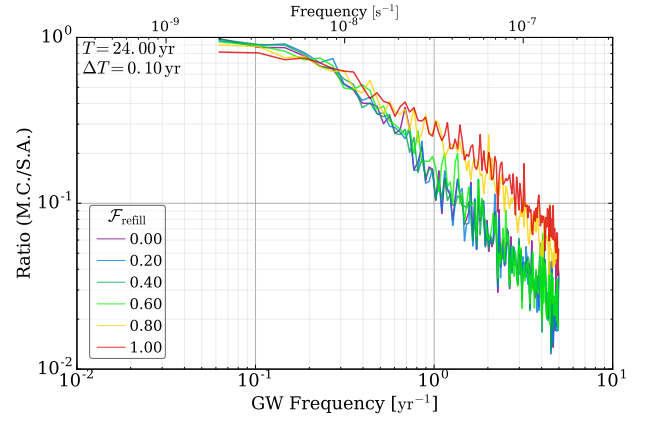


**Figure C4.** Ratio of the (median) MC-calculated GWB to that of the SA calculation, for zero-eccentricity and a variety of LC refilling fractions ( $\mathcal{F}_{\text{refill}}$ ). Finite-number effects, from few binaries in each bin, cause the strong deviation between Semi-Analytic (SA) and MC calculations at higher frequencies. This effect is somewhat alleviated by effective LC refilling ( $\mathcal{F}_{\text{refill}} \geq 0.8$ ) where the total number of coalescing binaries is increased.

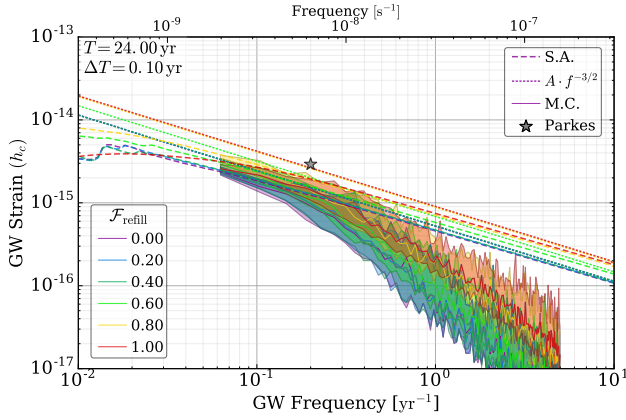


**Figure C3.** Monte-Carlo (MC) calculated GWB for a variety of different LC refilling fractions ( $\mathcal{F}_{\text{refill}}$ ), with median lines (solid) and one-sigma contours shown. Both the full (dashed) and power-law (dotted) SA models are also plotted. More efficient LC refilling means more binaries coalesce, causing the GWB amplitude to increase. An always full LC causes increased attenuation at lower frequencies: apparent at  $f \lesssim 0.1 \text{ yr}^{-1}$ . The steepening of the spectral index at higher frequencies due to finite-number effects is also apparent, but for  $\mathcal{F}_{\text{refill}} \geq 0.8$ , the effect is somewhat remediated.